



Effect of Laser Surface Processing on the Microstructure Evolution and Multiscale Properties of Atmospheric Plasma Sprayed High-Entropy Alloys Coating

Himanshu Kumar¹ · Gaurav A. Bhaduri² · S. G. K. Manikandan³ · M. Kamaraj⁴ · S. Shiva¹

Submitted: 30 August 2022 / in revised form: 20 October 2022 / Accepted: 25 October 2022 / Published online: 15 November 2022
© ASM International 2022

Abstract Two types of high-entropy alloys (HEAs) AlCrCoFeNiTi and FeCrCoNiW_{0.3} + 5 at.% C are fabricated using atmospheric plasma spray (APS) technique. Laser surface processing (LSP) is performed on the developed alloys using Nd:YAG pulsed laser. Post processing the surface roughness of the alloys are reduced by ~ 29%. The impact of laser surface processing reveals the presence of a single BCC phase and FCC phase with the evolution of more W-rich and Cr-rich carbides in AlCrCoFeNiTi and FeCoCrNiW_{0.3} + 5 at.% C coatings, respectively. The microstructural study exhibits the formation of lamellar microstructure with minimum pores and interlaminar cracks. Post laser processing the microhardness of both the APS coated alloys are increased by 5%, nanoindentation results reveal an increase in the average elastic modulus (Er) by 12%, and average nanohardness by 18%. The FeCoCrNiW_{0.3} + 5 at.% C coatings achieved

maximum wear resistance of 39.71% among the two alloys, indicating the improvement achieved through laser processing. Also the observed improvements in surface morphology of both the alloys are reported.

Keywords atmospheric plasma spray · coatings · high entropy alloy · laser processing · tribological properties

Introduction

High-entropy alloys (HEAs) contain five or more principle elements in equiatomic or near equiatomic percentage (at.%). The atomic percentage of each principle element may vary between 5 and 35 (Ref 1, 2). Recently, a lot of interest in HEA is seen mainly due to its high entropy of mixing ($\Delta S_{\text{mix}} \geq 1.5R$; where R is the universal gas constant), which is attributed to the formation of a single solid solution having either face-centered cubic (FCC) or body-centered cubic (BCC) or hexagonal closed pack (HCP) phase without any intermetallic phase formation. HEA is also known for their excellent mechanical properties such as wear resistance and microhardness (Ref 3-6), making it a promising candidate for various applications such as aerospace, defense, cryogenics, and surface engineering (Ref 7-9). The use of transition metal in the alloy system prevents the formation of the intermetallic phase and complex phases in the alloy (Ref 10). It has been observed that the addition of W and C in HEAs enhances the wear resistance and hardness (Ref 11, 12). Moreover, the segregation of the refractory element (W) and interstitial element (C) may occur at the grain boundary using the casting route (Ref 11).

The CoCrFeNi quaternary alloy consists of a single-phase FCC structure with low hardness, which limits its

This article is part of a special topical focus in the *Journal of Thermal Spray Technology* on New and Emerging Markets in Thermal Spray. The issue was organized by Dr. Andrew Vackel, Sandia National Laboratories; Dr. John Koppes, TST Engineered Coating Solutions; Prof. Bertrand Jodoin, University of Ottawa; Dr. Dheepa Srinivasan, Pratt and Whitney; and Prof. Shrikant Joshi, University West.

✉ S. Shiva
shiva.sekar@iitjammu.ac.in

- ¹ Laboratory for Advanced Manufacturing and Processing, Indian Institute of Technology Jammu, Jammu, India
- ² Process Intensification and Nanoscale Advanced Materials Laboratory, Indian Institute of Technology Jammu, Jammu, India
- ³ Indian Space Research Organization Propulsion Complex, Mahendragiri, India
- ⁴ Department of Metallurgical and Materials Engineering, Indian Institute of Technology Madras, Chennai, India

wide application (Ref 13). In order to overcome this limitation, the composition and crystal structure of the system is changed by addition of various elements such as Al, Cu, Mn, V, Pd, B, Mo and Ti (Ref 14–21). It has been observed that incorporating Al in CoCrFeNi alloy transforms the FCC to BCC structure. The movement of dislocation lattice in the BCC structure is less as compared to the FCC structure; therefore, BCC structure has lower plasticity and an improved hardness. However, addition of a high amount of Al leads to the formation of a brittle BCC phase making it undesirable for wear resistance (Ref 22). Furthermore, a substantial increase in hardness can be attained due to the formation of the intermetallic phase by addition of Ti in CoCrFeNi (Ref 23). The enhanced wear resistance and improved hardness have also been observed for addition of Ti (Ref 24, 25).

Currently, HEAs are being produced by various thermal spray techniques, such as high-velocity oxy-fuel (HVOF), high velocity air fuel (HVAF), Arc spray, Flame spray (Ref 26, 27), plasma spray (Ref 28–30), detonation gun spray and cold spray (Ref 29, 31). Recently, there have been multiple reports on comparing the mentioned methods and understating the advantages as well as the limitations of each of these methods. It has been observed that the various thermal spray techniques was used to synthesized variety of alloys such as CrMnFeCoNi (Ref 27), FeCoCrAlNi (Ref 28), CoCrFeMnNi (Ref 29), NiCoCrAlSi (Ref 30), AlCrFeCoNi (Ref 31) and AlCoCrFeNiTi (Ref 24) to name a few. Among all, the APS coated high-entropy alloy exhibits the superior hardness and wear resistance properties as compared to substrate material. Additionally, APS is a superior method to produce HEAs coatings for high-temperature applications (Ref 32, 33). APS facilitates a higher working temperature ($\sim 16,000$ °C), excellent wear resistance and higher tensile strength (8000–10,000 psi) (Ref 32, 34). APS sprayed AlCoCrFeNiTi exhibits a higher yield strength, ultimate tensile strength, and wear resistance (Ref 35, 36). Moreover, As casted FeCrCoNiW_{0.3}+ 5 at.% C alloy displays good oxidation resistance (Ref 11).

As a surface modification technique, laser cladding is used to improve surface defects and wear resistance (Ref 17). Furthermore, laser surface processing (LSP) has recently been applied to enhance the surface properties such as decreasing surface roughness and porosity, increasing wear resistance, corrosion resistance, and adhesion between surfaces of metallic components (Ref 37–42). LSP leads to an enhanced homogeneity of phase distribution, a reduced porosity and formation of new phases. The process being surface-sensitive does not affect the properties of the bulk material (Ref 38). By changing the operation mode of the laser, between pulsed or continuous, the penetration depth and dilution level can be

accurately controlled. Additionally, by choosing appropriate laser processing conditions, the material properties on the surface can be modified for any desired applications (Ref 39). Moreover, the grain boundary strengthening mechanism enhances the wear characteristics of the coatings. It has been observed that laser remelting of HEAs leads to a significant improvement in hardness and wear resistance. These coating have lower porosity with the formation of a single solid solution phase (Ref 40–42).

The effect of laser surface processing on AlCrCoFeNiTi and FeCrCoNiW_{0.3}+ 5 at.% C HEAs is yet to be explored to the best of our knowledge. In the present study, LSP is used to improve the surface property of the coating produced by atmospheric plasma spraying (APS). Initially both the HEA, i.e., AlCrCoFeNiTi and FeCrCoNiW_{0.3}+ 5 at.% C was coated on the stellite substrate using the APS technique. Subsequently, APS coated HEA sample is subjected to laser surface processing. The effects of laser surface processing on surface oxidation, bonding, surface roughness, microstructure, microhardness, physical properties and wear properties were investigated in detail and compared with as-sprayed alloys.

Experimental Procedure

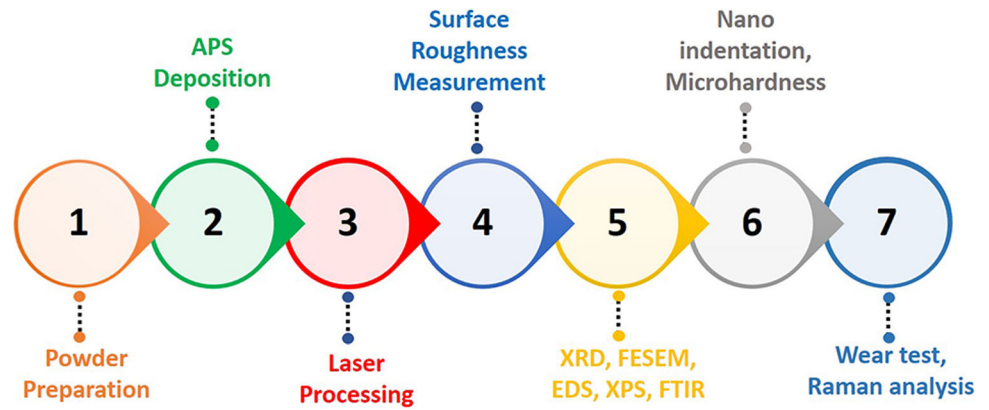
Preparation of High Entropy Alloy Powder

High purity powder 99.5% for Al, 99.8% for Co, 99% for Cr, 98% for Fe, 99.8% for Ni, 99.5% for Ti, 98% for W and 99% for C was procured from Orion Metal Powder Pvt. Ltd., India, having a particle size of 10–50 μm . Powders with a spherical form were favored over other shape for better alloy deposition efficiency. In order to keep powder particles from aggregating together, stearic acid was used. A table-top mixer (ALPHIE, ALPHIE-3) is used to pre-mix the powders at 40 rpm for 12 h for both alloy compositions. The detailed chemical composition of both alloy coatings is given in our previous work (Ref 34). Moreover, to reduce the moisture content and impurities, the powder particle is heated up before it is deposited. A process chart of the preparation and test carried out in the current manuscript is given in Fig. 1.

APS Coating Operation

A 100 mm \times 100 mm \times 3 mm stellite substrate was ultrasonically cleaned and then immersed in an ethanol bath before the deposition. APS method was used to deposit AlCrCoFeNiTi and FeCrCoNiW_{0.3}+ 5 at.% C HEAs on the substrate. Over 20 μm of sample roughness was used to ensure good coating-to-substrate adhesion (Ref 31). The deposition is accomplished with the help of an

Fig. 1 Process chart for preparation and test carried out in current work



APS radial spray gun (METCO 9 MB, India). The robotic arm moves the plasma torch assembly transversely over the substrate holder. The plasma torch moved at a speed of 100 m min^{-1} in the transverse direction. Spray velocity and temperature have an impact on the splat behavior, which results in a change in microstructure. As the main plasma gas, Argon (Ar) flowed at 42.1 slpm (standard litre per minute), while H_2 gas flowed at 2.35 slpm to obtain the targeted plasma jet temperature. In this experiment, the voltage and current used in the spraying were 60 V and 530 A, respectively, with a transverse speed of 100 m/min. A 6-slp high-pressure carrier gas (Argon) transports powder from the hopper to the convergent portion of the GH-type thermal plasma nozzle. The detailed process parameters used for deposition are given in our previous work (Ref 34). The deposited layer’s thickness was determined to be $200 \mu\text{m}$ using a ten-point calibration system.

Laser Surface Processing Operation

The sample was cleaned with ethanol before laser surface processing after AlCrCoFeNiTi and FeCrCoNiW_{0.3} + 5 at.% C HEA alloys were APS sprayed on a stellite substrate. The Nd: YAG laser (Quanta-Ray, India) was utilized in Q-switched mode for single-track LSP, with the process parameter used for LSP shown in Table. 1. An example of a pulsed laser is a Q-switched laser. Pulses of energy released at a specific pulse repetition frequency define its output. The Q-switch, a nonlinear crystal, is located within the laser’s cavity. After a certain number of repetitions, it will finally open. When the Q-switch is opened, a powerful laser pulse is generated, increasing the depth of penetration. The Q-switched pulse laser was shown to be preferable to the continuous laser in the present research because it provides double the cooling time, thus reducing the risk of laser ablation. A 210 W power laser used for processing both the APS coating with a scanning speed of 6 mm/s. In order to keep the surface from oxidizing, argon gas is used as a shielding gas. In Fig. 2, a schematic representation of the LSP process is presented.

Table 1 Optimized laser processing parameters for AlCrCoFeNiTi and FeCrCoNiW_{0.3} + 5 at.% C HEA alloy

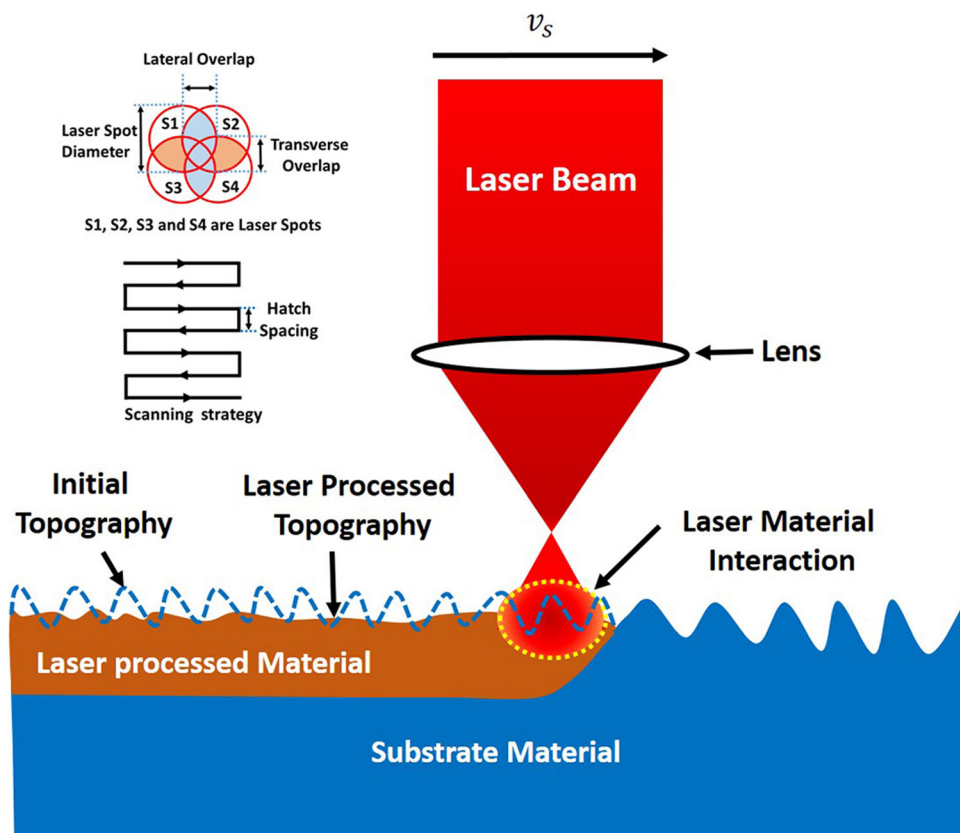
Parameter	Unit	Value
Laser power	W	210
Pulse frequency	Hz	10
Pulse duration	ns	9
Spot diameter	mm	2
Scanning rate	mm/s	6
Mode of operation	...	Q Switch
Laser wavelength	nm	532
Overlap	%	90

Coating Characterization

After the laser surface processing sample was polished and etched, with prepared according to ASTM: E1920 standard. The sample mold is made using commercially available cold mounting and then grinded using a belt grinder BGGP (METCO Ltd., India). The microstructure and microhardness indentation were revealed after mechanical polishing on the laser-processed materials using a variable speed polisher BAINPOL-VTD individual drive (METCO Ltd., India).

The surface morphology and microstructure of the HEAs coating were examined using a field emission scanning electron microscope (FESEM) (JEOL, JSM 7900F) before and after laser processing at a working voltage of 15 kV. Energy dispersion x-ray spectroscopy (Oxford Instruments) was used to examine the chemical composition of the coated AlCrCoFeNiTi and FeCrCoNiW_{0.3} + 5 at.% C HEAs and the XPS data were obtained utilizing (Nexsa™, Thermo Scientific,) instrument. The collected data were calibrated by assigning the most intensive peak to adventitious carbon at 284.5 eV. The XPS data were analyzed using WinSpec software. The background used for the fitting was Shirley and subtracted

Fig. 2 Schematic representation of laser surface processing



for ease of fitting. All peaks were fit using mixed singlet. The carbon content in the coating was determined using the CHNS analyser (Elementor, UNICUBE). The functional groups of both LSP HEAs coatings were confirmed by FTIR spectroscopy (Nicolet iS50, Thermo Scientific). The optical surface profilometer (OLYMPUS, DSX510) was used to evaluate the surface roughness of both HEAs before and after laser processing with a cutoff length of 300 μm and a surface area of 399 μm^2 . X-ray diffraction spectroscopy (Empyrean, Malvern Panalytical,) Bragg–Brentano method, Cu- source was used to determine the coating's crystal structure and phase orientation with 10 s dwell time and 0.5-degree scanning step. The corresponding peak has been identified and compared to the standard from the powder diffraction dataset from the ICDD (International Centre for Diffraction Data). Microhardness of both HAEs was determined by applying a 200 gf load for 15 s of dwell time using the Vickers microhardness tester (Falcon 400, Innova Test). Nanoindentation was performed using (FoundatiONE-Multiscale testing system, India) under a load of 5000 μN .

Samples were polished with sandpaper of various grit sizes and cleaned in ethanol before the wear test analysis. An Al_2O_3 ball with a diameter of 10 mm was used as a counter body against a smooth coated surface in a ball-on-disc tribometer (POD 4.0, Ducom Instruments). The

experiment is carried out under dry sliding conditions at 25 $^\circ\text{C}$ with a load of 5 N. The speed of the disc was 600 rpm with a wear track diameter of 10 mm. The Raman analysis was performed on the worn surface post-wear test using Raman Spectrometer (R532, Enspectr) with a working wavelength of 532 nm. The background for the Raman data was subtracted using a liner background and the data were normalized for proper identification of peaks.

Results and discussion:

Powder Characterization

To produce a pore-free, higher-density coating, spherical-shaped powder particles were chosen over flaked-shaped particles. Figure 3(a) and (b) shows the powder morphology AlCrCoFeNiTi and FeCrCoNiW_{0.3} + 5 at.% C alloys, respectively. Figure 3 reveals that the majority of powder particles are spherical.

The size of the powder particles ranged from 10 to 50 μm . Figure 4 shows the particle distribution of different AlCrCoFeNiTi and FeCrCoNiW_{0.3} + 5 at.% C HEA constituents, which shows that the majority of the powder particle size ranges from 30 to 40 μm .

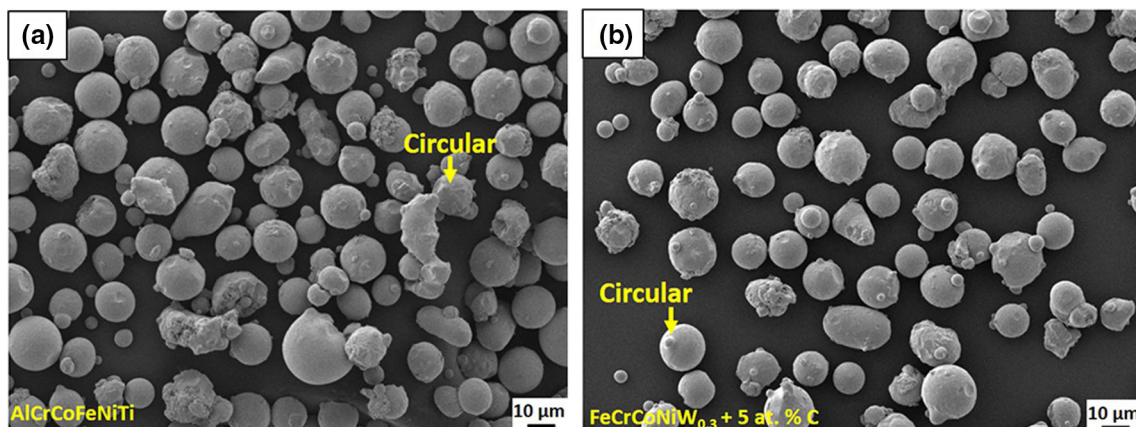


Fig. 3 FESEM powder particle morphology of (a) AlCrCoFeNiTi and (b) FeCrCoNiW_{0.3} + 5 at.% C

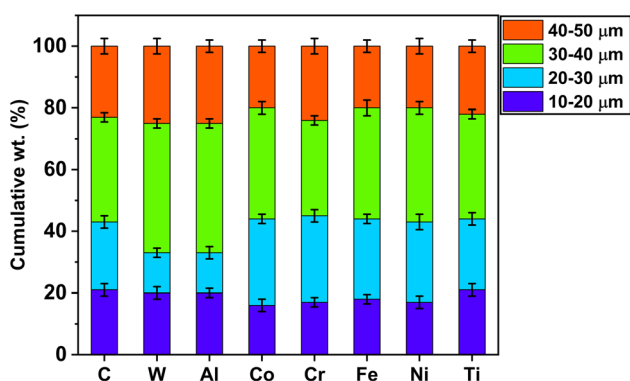


Fig. 4 Particle distribution of different AlCrCoFeNiTi and FeCrCoNiW_{0.3} + 5 at.% C HEA constituents

Surface Characterizations

Samples of AlCrCoFeNiTi and FeCrCoNiW_{0.3} + 5 at.% C APS coatings were subjected to optical profilometer studies to determine the difference in line surface roughness (Ra) and areal surface roughness (Sa) after and before laser processing. Table 2 shows the pre- and post-laser sample areal surface roughness values. Both alloys line roughness profiles are shown in Fig. 5. Variations in the line roughness profile (e.g., peaks and valleys) were identified before and after laser processing. Figure 5(a) shows the 2D line roughness profile of the AlCrCoFeNiTi alloy and the LP_AlCrCoFeNiTi sample. The AlCrCoFeNiTi and LP_AlCrCoFeNiTi samples exhibit line roughness of 6.05 μm, and 2.52 μm, respectively. In addition, FeCrCoNiW_{0.3} + 5 at.% C and LP_FeCrCoNiW_{0.3} + 5 at.% C sample displays a substantial variation in the 2D line profile, which is equivalent to 12.07 μm and 3.47 μm, respectively, (Fig. 5(b)). The results show that laser surface processing improves homogeneity and reduces alloy surface undulation in both alloys by localized heating, melting, and solidification of the surface.

The areal roughness value (Sa) after laser processing is significantly reduced in both the APS coatings, with the decrease in roughness attributed to localized heating, melting and solidification of the surface. Figure 6 shows the 3D surface roughness profiles of both samples. The AlCrCoFeNiTi and FeCrCoNiW_{0.3} + 5 at.% C APS coating exhibits needle-type spikes before laser processing, as illustrated in Fig. 6(a) and (c). The 3D roughness profile homogeneity is smoothed and homogenized after laser processing, as illustrated in Fig. 6(b) and (d). Whereas, the surface roughness of LP_AlCrCoFeNiTi sample decreases by 29.03%, that of LP_FeCrCoNiW_{0.3} + 5 at.% C alloy decreases by 29.59% after laser processing. Laser surface processing facilitates localized heating and rapid solidification attributed to lower surface defects, porosity and lower surface roughness. Both alloys reduced surface roughness improves wear resistance by reducing friction and asperity contact in sliding environments. The surface roughness analysis results are listed in Table 2.

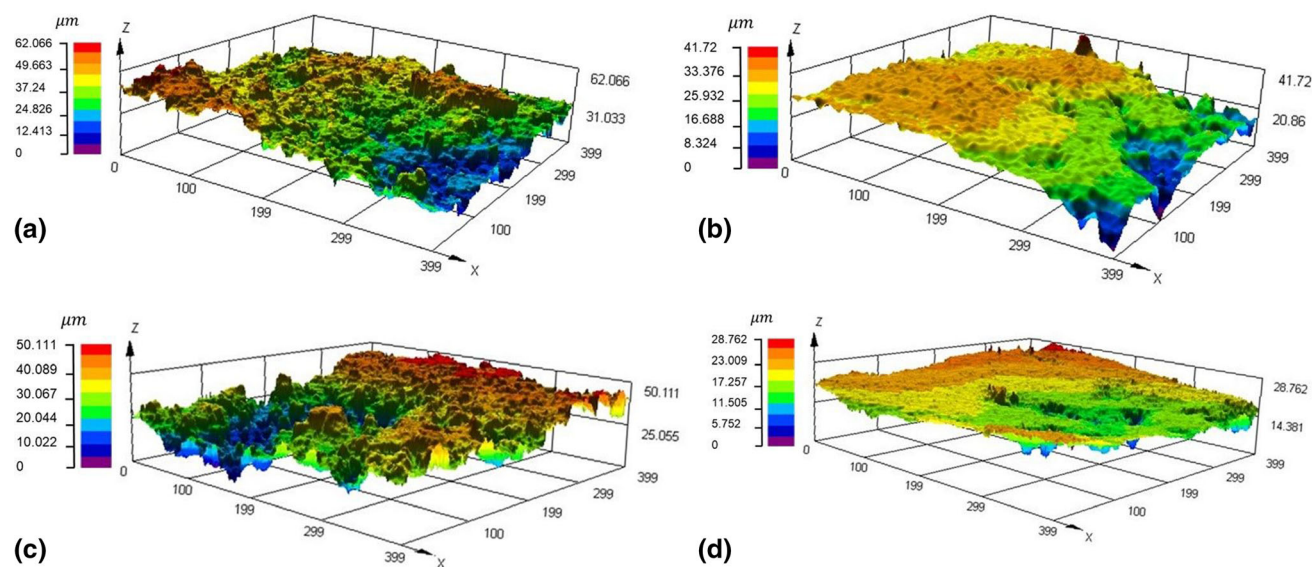
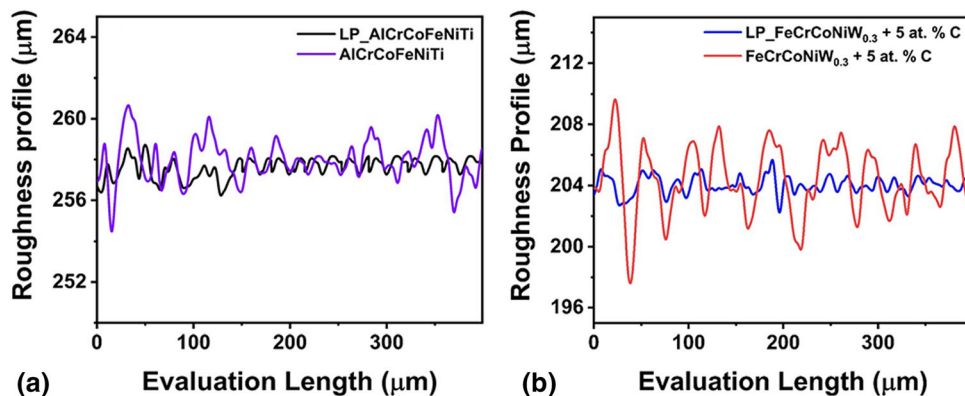
FESEM cross-sectional image of laser processed AlCrCoFeNiTi and FeCrCoNiW_{0.3} + 5 at.% C APS coating is shown in Fig. 7(a) and (b), respectively. Both APS coating exhibit superior metallurgical bonding between the coating and substrate. There are no cracks or voids observed at the interface in both the APS coating. The dilution percentage is computed using the following equation to investigate the coating and substrate dilution levels.

$$\text{Dilution}(D)\% = \frac{A_{ms}}{A_o + A_{ms}} \times 100 \tag{Eq 1}$$

where, A_{ms} represents the area of the melted substrate during laser processing and A_o is area of overlay coating. The melted substrate thickness is measured as 20.8 μm, and 18.5 μm in the case of laser processed AlCrCoFeNiTi and FeCrCoNiW_{0.3} + 5 at.% C APS coating, respectively. The overlay coating thickness is measured as 199.54 μm and 201.32 μm. The dilution percentage is evaluated over a

Table 2 Surface roughness of the deposited AlCrCoFeNiTi and FeCrCoNiW_{0.3} + 5 at.% C HEA APS coatings before and after laser processing

Sample	S _a (μm) Before laser processing	S _a (μm) After laser processing	Decreased surface roughness (%)
AlCrCoFeNiTi	7.37 ± 0.21	5.23 ± 0.21	29.03%
FeCrCoNiW _{0.3} + 5 at.% C	6.42 ± 0.31	4.52 ± 0.31	29.59%

Fig. 5 2D line roughness profile of (a) AlCrCoFeNiTi and, (b) FeCrCoNiW_{0.3} + 5 at.% C APS coatings before and after laser processing**Fig. 6** 3D surface roughness profile of the (a) as sprayed AlCrCoFeNiTi, (b) laser processed AlCrCoFeNiTi, (c) as sprayed FeCrCoNiW_{0.3} + 5 at.% C, and (d) laser processed FeCrCoNiW_{0.3} + 5 at.% C APS coatings

width of 1 mm. The dilution percentage is calculated as 9.43% and 8.41% in case of laser processed AlCrCoFeNiTi and FeCrCoNiW_{0.3} + 5 at.% C APS coating, respectively. The coating dilution level is controlled by the laser power, scanning speed, stand-off distance, and mode of operation of the laser. In general, high-temperature spraying procedures increase porosity in coatings, resulting in a large number of voids, which act as fracture initiation sites. However, the formation of pores in the coating can be reduced by utilizing laser processing and laser-optimized process parameters. In the interface region, the coating's

decreased porosity and fewer interlaminar cracks near the interface region. However, a dilution level study revealed a strong metallurgical bonding between coating and substrate.

Phase Analysis

Figure 8 shows the XRD results of as-sprayed and laser processed AlCrCoFeNiTi and FeCrCoNiW_{0.3} + 5 at.% C HEA APS coatings. The diffraction results of the LP_AlCrCoFeNiTi coating show two BCC solid solution

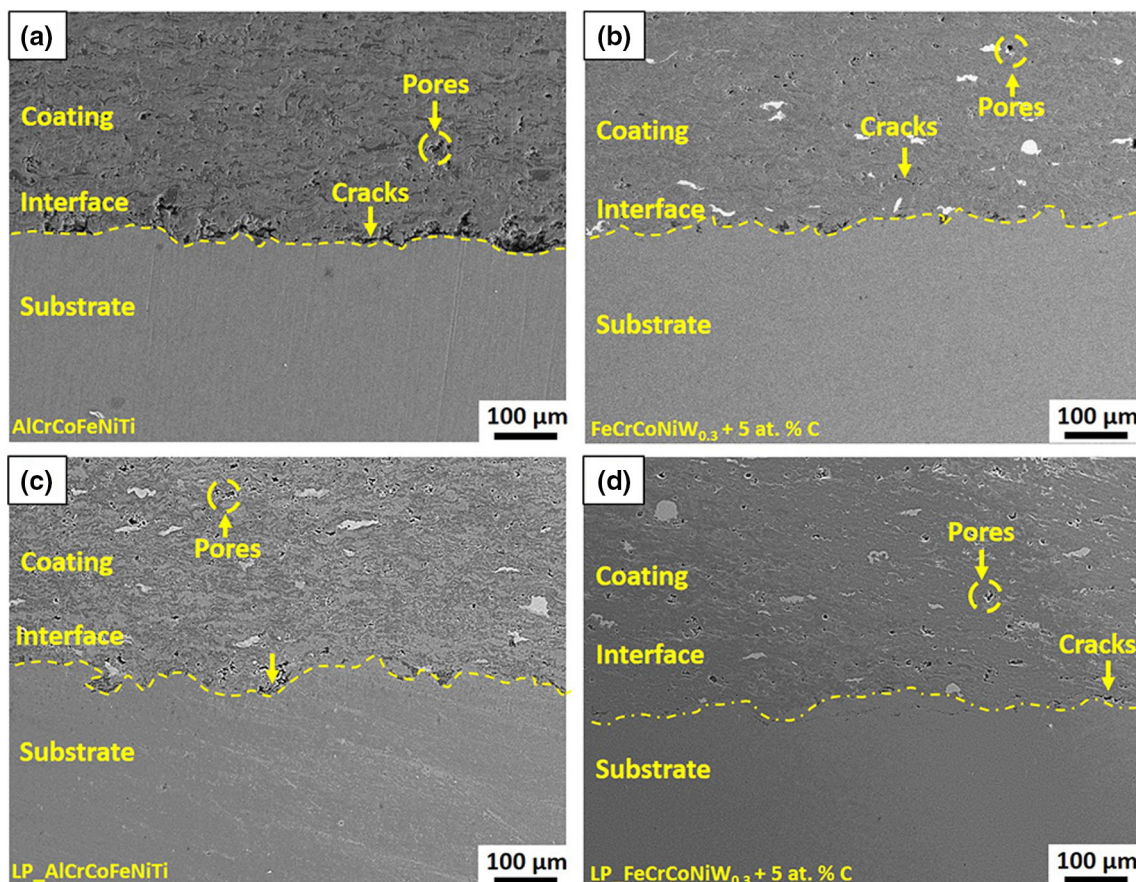


Fig. 7 FESEM image of coating cross section of (a) as sprayed AlCrCoFeNiTi, (b) as sprayed FeCrCoNiW_{0.3} + 5 at.% C (c) laser processed AlCrCoFeNiTi, and (d) laser processed FeCrCoNiW_{0.3} + 5 at.% C APS coatings

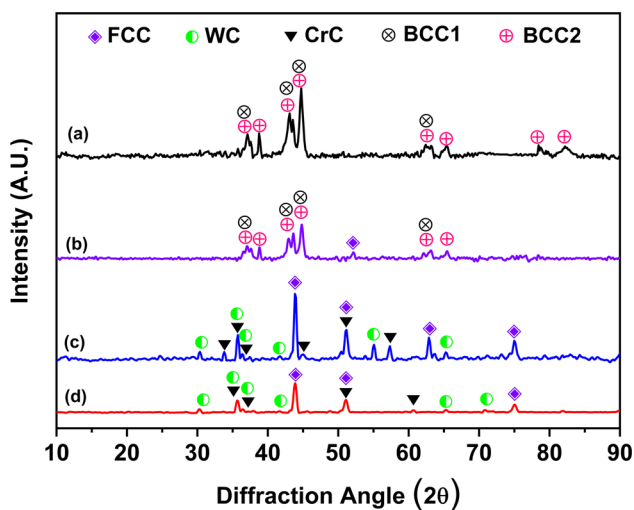


Fig. 8 XRD patterns of (a) LP_ AlCrCoFeNiTi, (b) AlCrCoFeNiTi, (c) LP_ FeCrCoNiW_{0.3} + 5 at.% C and (d) FeCrCoNiW_{0.3} + 5 at.% C APS coatings

phases of FeCr (BCC1) and AlNi (BCC2); both peaks were separated by the shift in the lattice parameter from 2.93 to 2.94 Å attributed to the addition of Ti. The BCC (BCC1)

phase denotes diffraction peaks with high intensities, whereas the BCC (BCC2) phase denotes peaks with lesser intensities. In XRD, the Al-rich phase may be associated with the BCC1 phase (ICDD card no – 00–006–0694). The high-intensity BCC2 phase is overlapped and widens, making it difficult to see the low-intensity BCC2 phase (ICDD card no: 03–065–4198). As compared to the as-sprayed coating, more BCC phases developed in the LP_AlCrCoFeNiTi alloy, whereas minimal FCC phases were eliminated.

X-ray diffraction pattern for LP_ FeCrCoNiW_{0.3} + 5 at.% C HEA coating exhibit the one FCC (ICDD card no – 00–047–1417, 00–033–0397 and 44–0962) solid solution phase containing two carbide phases, W-rich carbide represented as (WC) (ICDD card no – 003–1096 and 020–1315) and Cr rich carbide (ICDD card no – 035–0783, 35–0804 and 036–1482) indicated as (CrC). It is clear from the XRD results that there is no change in the crystals structure of the APS coated and LP samples. Because of the low carbon content, the peaks of W and Cr-rich carbides closely resemble those of W₂C type carbide and Cr₂₃C₆ type carbide. On comparing the APS-sprayed coating with the laser-treated coating it was observed that there is an

increase in the carbides phase in the laser-treated coatings. This may be due to the diffusion of carbon in Cr and W (Ref 11).

Microstructural analysis

Laser-treated AlCrCoFeNiTi HEA coating deposited by the APS technique, (Fig. 9a, b) has a lamellar microstructure. FESEM images showed fewer pores on the laser-processed surface of the sample than on the as-sprayed one (Fig. 9a, b). Generally, laser processing is known to cause (CrMnFeCoNi) coating to hot crack (Ref 42); however, in the present case, FESEM examination shows minimum interlaminar cracks in the laser-treated sample.

There are three distinct regions present in the laser-processed AlCoCrFeNiTi APS coating (Fig. 9b). The point EDS confirmed that the a_2 region is associated with Al-rich phase, whereas the a_3 region indicates Cr-rich phase with Al depletion, and the a_1 region denotes rich in Ti-rich oxides.

As-sprayed FESEM image of the FeCrCoNiW_{0.3} + 5 at.% C APS coating is shown in Fig. 9(c). It comprises

three distinct regions. Point EDS confirm that the a_2 region is rich in CrC and Fe phase, whereas the a_3 region is rich in WC phase and the a_1 region is rich in Fe, Ni and Co phase. Due to the dispersion of carbon in Cr and W, WC and CrC phases are found. Figure 9(d) shows a FESEM image of a laser treated FeCrCoNiW_{0.3} + 5 at.% C HEA alloy coating denoted as (LP_FeCrCoNiW_{0.3} + 5 at.% C) with same distinct phases as-sprayed one. LP_FeCrCoNiW_{0.3} + 5 at.% C APS coating microstructure revealed the more homogeneous distribution of phase, as shown in Fig. 9(d).

Prior to and after laser processing, the chemical constituent elements of AlCrCoFeNiTi and FeCrCoNiW_{0.3} + 5 at.% C APS coating was identified using the area EDS and point EDS. Table 3 shows the EDS findings at several locations marked in Fig. 9. Moreover, the carbon content in the FeCrCoNiW_{0.3} + 5 at.% C and LP_FeCrCoNiW_{0.3} + 5 at.% C is found to be 7 and 6.2 at.%, respectively. The EDS results demonstrate a perfect correlation between the nominal compositions of each element used in coating synthesis. The homogenous dispersion of elements attributed to a little change in the atomic percentage of Al, Cr, Fe, Ni, Ti, W, and C after laser processing. Because of the high melting temperature and oxygen formation on the

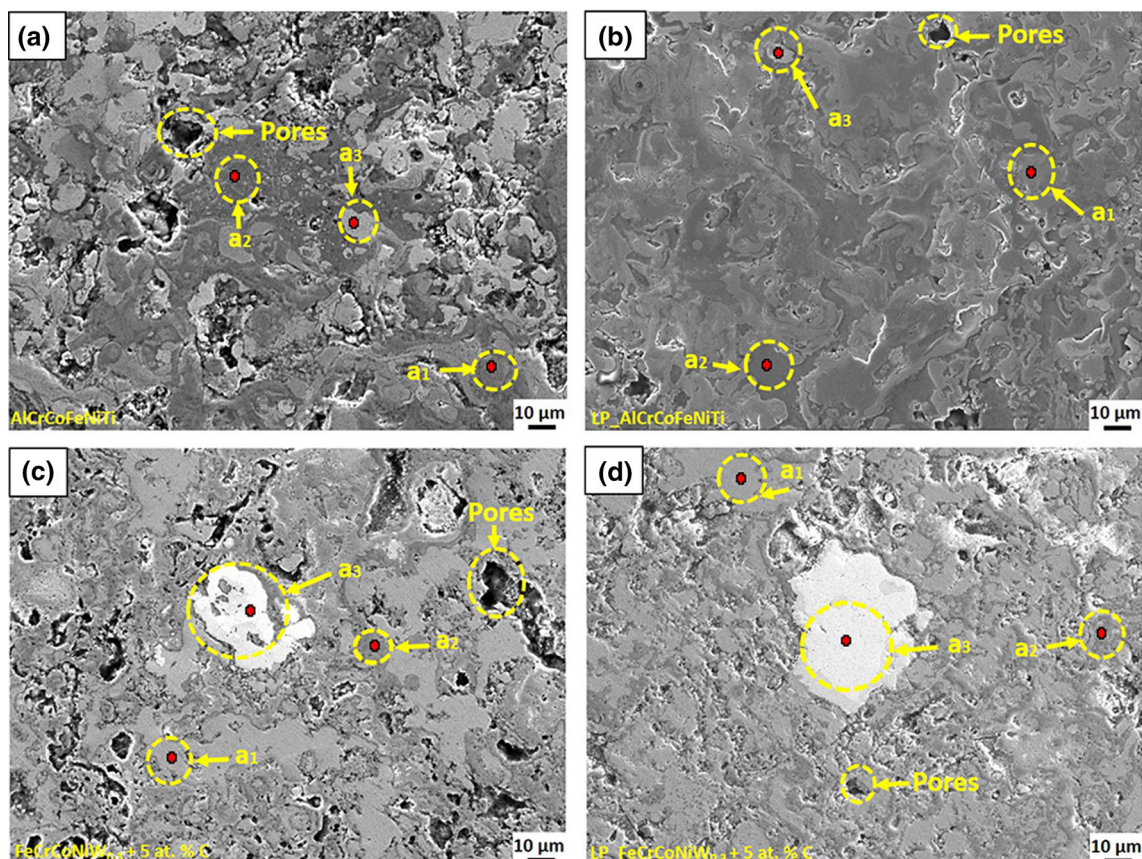


Fig. 9 FESEM cross-sectional image of (a) as sprayed AlCrCoFeNiTi, (b) LP_AlCrCoFeNiTi, (c) as sprayed FeCrCoNiW_{0.3} + 5 at.% C, and (d) LP_FeCrCoNiW_{0.3} + 5 at.% C APS coatings

Table 3 Chemical composition of AlCrCoFeNiTi and FeCrCoNiW_{0.3} + 5 at.% C APS coatings before and after laser processing

Locations	Composition (at.%)							
	Al	Cr	Co	Fe	Ni	Ti	W	O
Whole Area (Fig. 9 a)	14.39	14.4	14.56	13.82	14.77	14.46	...	13.6
a ₁ region (Fig. 9 a)	6.07	2.68	2.71	2.46	2.55	70.78	...	12.75
a ₂ region (Fig. 9 a)	47.52	5.01	6.44	6.37	6.44	14.21	...	14.01
a ₃ region (Fig. 9 a)	4.29	42.13	4.29	15.03	14.22	8.00	...	12.04
Whole Area (Fig. 9 b)	14.24	14.34	14.36	14.24	14.46	14.46	...	13.90
a ₁ region (Fig. 9 b)	4.46	27.12	4.14	8.69	6.90	33.65	...	15.04
a ₂ region (Fig. 9 b)	35.43	11.94	5.35	11.21	7.49	12.45	...	16.13
a ₃ region (Fig. 9 b)	4.97	15.08	11.98	28.31	18.04	5.51	...	16.11
Whole Area (Fig. 9 c)	...	19.42	18.67	19.01	19.54	...	3.7	19.66
a ₁ region (Fig. 9 c)	...	8.42	15.89	32.13	26.24	...	0.23	17.09
a ₂ region (Fig. 9 c)	...	36.57	10.41	22.59	11.29	...	1.15	17.99
a ₃ region (Fig. 9 c)	...	12.20	2.37	2.50	1.04	...	64.17	17.72
Whole Area (Fig. 9 d)	...	18.62	18.62	18.81	19.02	...	4.28	20.65
a ₁ region (Fig. 9 d)	...	15.98	19.59	23.13	20.57	...	0.42	20.31
a ₂ region (Fig. 9 d)	...	31.60	11.98	23.76	10.57	...	2.09	20.00
a ₃ region (Fig. 9 d)	...	11.71	4.61	4.14	3.11	...	56.33	20.10

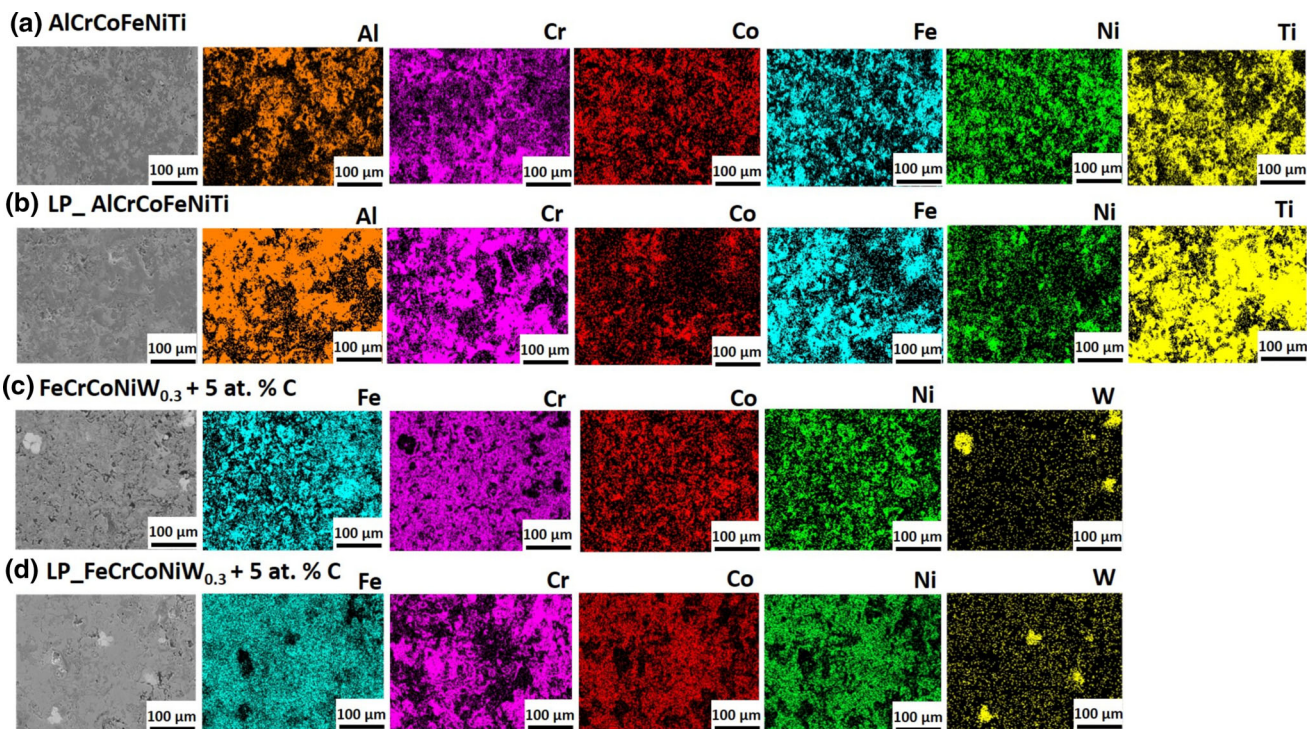


Fig. 10 EDS elemental mapping of (a) AlCrCoFeNiTi, (b) LP_AlCrCoFeNiTi, (c) FeCrCoNiW_{0.3} + 5 at.% C and (d) LP_FeCrCoNiW_{0.3} + 5 at.% C APS coatings

grain boundary, the atomic percentage of oxides was increased in laser-treated samples for both alloys. In addition, XPS tests were carried out to discover more about oxygen’s significance.

Figure 10 shows the results of an elemental mapping study performed using EDS on the alloy coatings before

and after laser processing. The distribution of all of the elements in the area may be seen via the use of elemental mapping. Figure 10(b) and (d) demonstrates that LP_AlCrCoFeNiTi and LP_FeCrCoNiW_{0.3} + 5 at.% C coatings constituents have a more homogenous distribution and are mixed well. However, LSP does not affect W due

to its higher melting temperature, and W can be seen as a particle phase. Due to the fast heating and solidification effects during LSP, a more uniform distribution of constituents is observed in contrast to the as-sprayed alloys.

Chemical Analysis of the Surface

AlCrCoFeNiTi alloy's carbon 1s spectrum can be split into three distinct peaks at 284.5, 285.9, and 288.2 eV, correspondingly as shown in Fig. 11(a). C 1s peaks at 285.9 eV and 288.2 eV indicate the alloy contains hydrocarbon compounds. The Al 2p peak at 73.0 eV may be attributed to metallic Al, whereas the peak at 73.5 eV indicates the existence of an AlNiO (Ref 43) alloy, and the peak at 74.5 eV can be attributed to Al₂O₃ (Ref 44). Ni 2p has three peaks at 854.0, 855.0, and 861.23 eV, respectively. NiO is responsible for the peak at 854.0 eV (Ref

46), whereas Ni(OH)_x is responsible for the peak at 855.0 eV (Ref 49). There is a Ni 2psat peak at 861.2 eV (Ref 46). Both the peaks at 575.6 and 576.8 eV of Cr 2p have been attributed to Cr oxides (Ref 45). The 779.8 eV Co peak may be attributed to Co₂O₃, whereas the 781.8 and 785.5 eV Co peaks can be attributed to Co₃O₄ and CoO, respectively (Ref 45). Both the Fe 2p peaks, 711.7 and 709.7 eV may be attributed to Fe₂O₃ and FeO, respectively (Ref 46). TiO₂ has two oxidation states, with peak energies of 457.9 and 456.2 eV, respectively (Ref 47). O 1s peak at 529.5 eV indicates the presence of several metal oxides, and the peak at 530.8 eV indicates the presence of both AlNiO and NiOH.

Post laser processing a minor changes are observed in LP_AlCrCoFeNiTi coating in contrast to as sprayed coating, as shown in Fig. 11(b). C 1s shows an additional peak at 283.5 eV suggests the presence of carbides. Al 2p peak

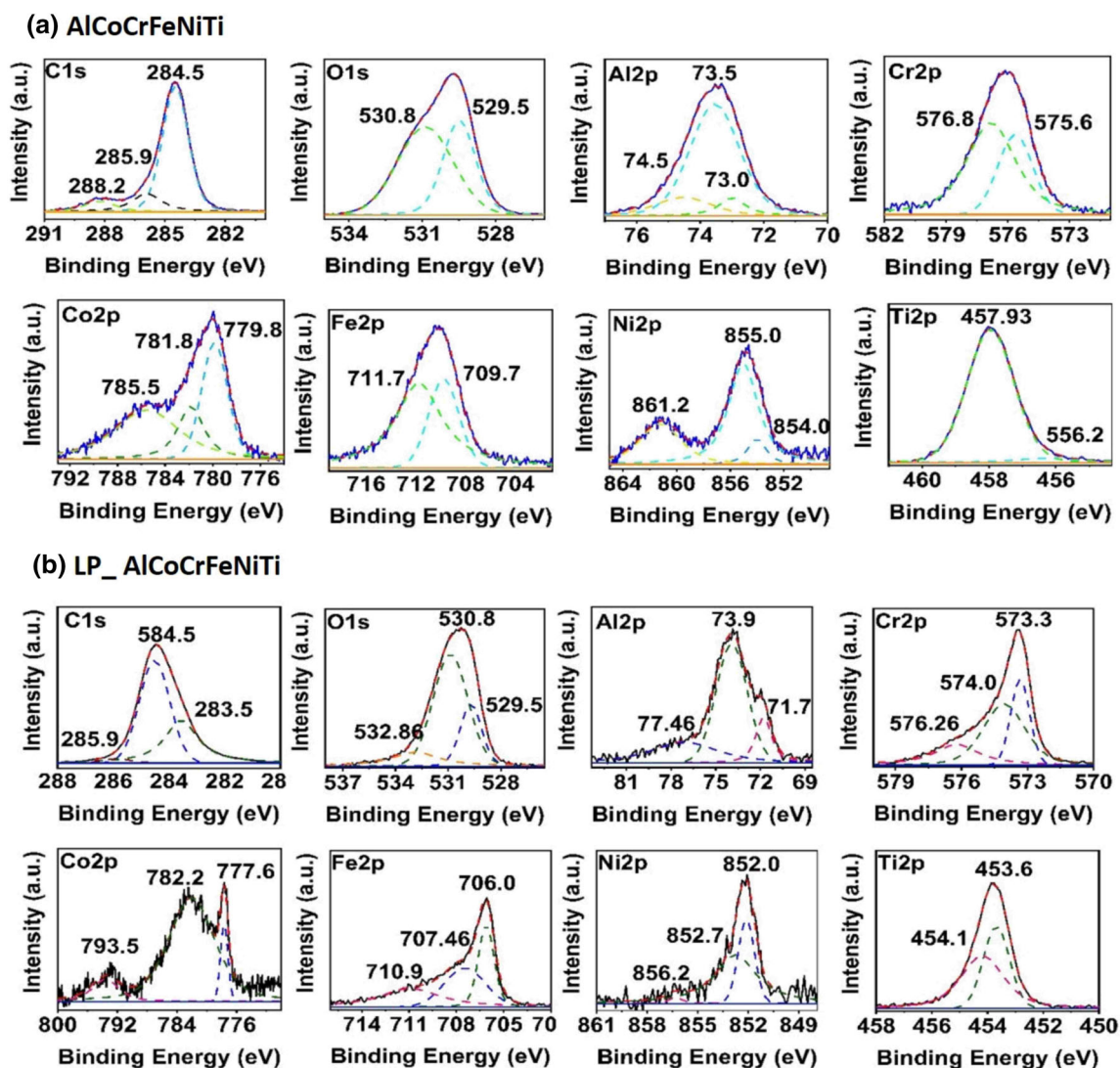


Fig. 11 XPS spectra of AlCrCoFeNiTi APS coating (a) before laser processing and, (b) after laser processing

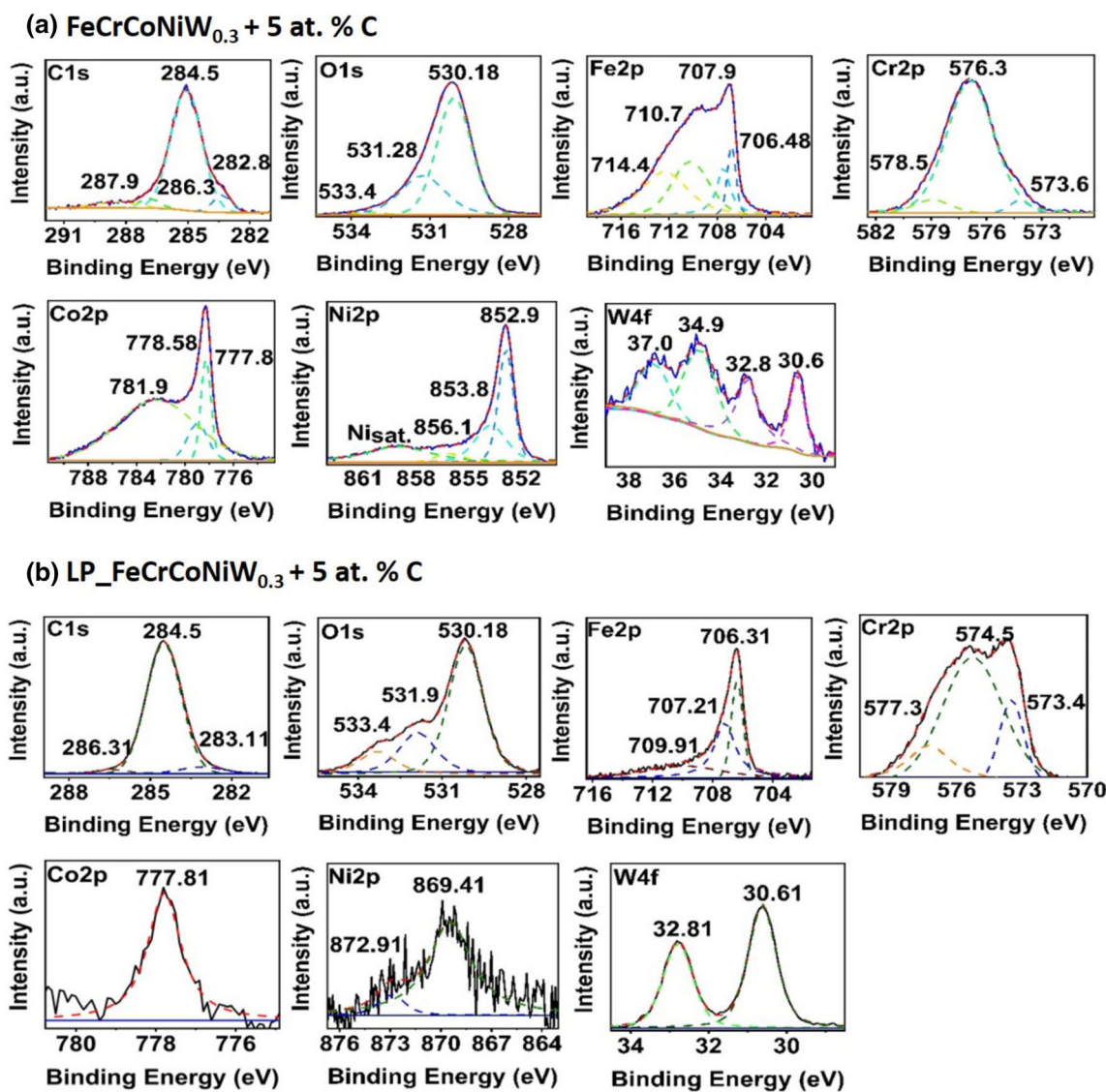


Fig. 12 XPS spectra of FeCrCoNiW_{0.3} + 5 at.% C APS coating (a) before laser processing and (b) after laser processing

at 71.7 eV can be assigned to metallic Al, 73.9 eV suggests the presence of AlNiO alloy (Ref 43), whereas the peak at 77.4 eV can be assigned to Al₂O₃ (Ref 44). The Ni 2p peak at 856.2 eV can be assigned to AlNiO (Ref 43), whereas the peak at 852.0 eV is assigned to NiTi (Ref 45), and 852.7 eV can be assigned to Ni⁰ (Ref 46). The Ti 2p peaks 453.6 eV and 454.1 eV can be assigned to Ti⁰ (Ref 47) and NiTi, respectively (Ref 45). The peaks of Cr 2p at 573.3 eV, 574.0 eV and 576.26 eV can be assigned to CrC, FeCr (Ref 48) and Cr₂O₃ respectively (Ref 46). The peaks of Fe 2p of 706.0 eV, 707.46 eV and 710.9 eV can be assigned to Fe⁰, FeCr (Ref 48) and Fe₂O₃ respectively (Ref 46). Co peaks at 77.6 eV, 782.2 eV and 793.5 eV are assigned to Co⁰, CoO, and Co^{sat}, respectively (Ref 46).

Pre laser processing FeCrCoNiW_{0.3} + 5 at.% C alloy's carbon 1 s peak is associated with carbide at 282.8 eV,

whereas chromium hydrocarbon complexes may be found at 286.3 and 287.9 eV as shown in Fig. 12(a). Three significant peaks at 530.18, 531.28, and 533.4 eV can be seen in the O 1 s spectrum. A variety of oxides of Cr, Fe, Ni, Co, and W may be responsible for the 530.18 eV peak (Ref 46). On the other hand, the peak at 531.2 eV suggests the alloy contains hydroxyl species. In the peak of Cr 2p peak at 573.6 eV, is correspond to chromium carbide (Ref 48), while, peak at 578.5 eV is associated with chromium hydrocarbon complex (Ref 47). The presence of CrO is inferred from the peak at 576.3 eV. The 777.8, 778.58, and 781.9 eV Co 2p peaks may be attributed to metallic Co, CoNi alloy (Ref 52), and Co(OH)_x, respectively (Ref 46). Three peaks of Ni 2p spectrum at 852.9 eV is allocated to CoNi alloy (Ref 51), whereas 853.8 and 856.1 eV are assigned to NiO and Ni(OH)_x, respectively (Ref 52). Fe 2p

peak at 706.4 eV may be attributed to metallic Fe, while the peak at 707.9 eV can be attributed to FeC, which corresponds to the 282.8 eV C 1 s peak. The other two peaks at 710.7 eV and 714.4 eV may be ascribed to Fe₂O₃ and FeOOH, respectively (Ref 46, 51). W 4f has two peaks, one at 30.6 eV and the other at 34.9 eV may be assigned to metallic W and WC, respectively (Ref 52).

Post laser processing FeCrCoNiW_{0.3} + 5 at.% C alloy exhibits minor changes in comparison to as sprayed counterpart, as shown in Fig. 12(b). The additional peak of carbon 1 s peak at 283.1 eV suggests the presence of carbides. The Cr 2p peaks at 573.4 and 577.3 eV can be assigned to chromium carbide (Ref 50), CrFe alloy (Ref 48) and chromium oxide, respectively. The Fe 2p peak at 707.2 eV confirms the presence of CrFe alloy (Ref 48), whereas the peaks at 706.3 eV can be assigned to metallic Fe (Ref 46, 51). One peak is observed for metallic Co at 777.8 eV and metallic W at 30.4 eV (Ref 52). Ni 2p shows the presence of metallic Ni at 869.41 eV and NiO at 872.91 eV (Ref 52).

AlCrCoFeNiTi and FeCrCoNiW_{0.3} + 5 at.% C HEA alloy's surface before and after laser processing was observed using Fourier transform infrared spectroscopy to detect molecular vibrational states as shown in Fig. 13. AlCrCoFeNiTi HEA coating's vibrational characteristics spectrum, with peaks ranging from 444 to 681 cm⁻¹, indicates the existence of different metal oxides such as Fe–O, Cr–O, Co–O, Ni–O, Ti–O, Al–O or Ni–O stretching mode on the sample surface as shown in Fig. 13 (Ref 53, 54). Similar findings were found in the preceding section's XPS investigation; both confirm the formation of various metal oxides at the coating surface. Vibration spectra show a Ti–O–Ti bond at 670–450 cm⁻¹ wavenumber (Ref 55). Characteristics spectrum presence at 1706 cm⁻¹ attributed to C = O stretching mode, although the spectra present at 1210 cm⁻¹ ascribed to the C = O stretching mode. Furthermore, the sequence of distinctive peaks between 1400 and 1600 cm⁻¹ shows Ti–O–C molecular vibration, which verifies the bonding between Ti and C (Ref 56). Vibrational spectra displayed at 1568, 1690 and 1727 cm⁻¹ were ascribed to C = O asymmetric stretching, C = O stretching and C = O stretching correspondingly, and spectra present at 2350 cm⁻¹ related to –O–C–O– bond (Ref 57). However, FTIR analysis of LP_AlCrCoFeNiTi sample does not have a significant deviation from the value assigned to the as-sprayed sample. Similarities can be seen between the FTIR and XPS findings. The quality of the coating was confirmed by the FTIR findings, which showed no impurities on the sample surface.

It can be seen in Fig. 13 that the FeCrCoNiW_{0.3} + 5 at.% C sample's distinctive vibrational spectrum has many peaks between wavenumbers 444 and 681 cm⁻¹. These peaks have been linked to metal oxides in stretching mode,

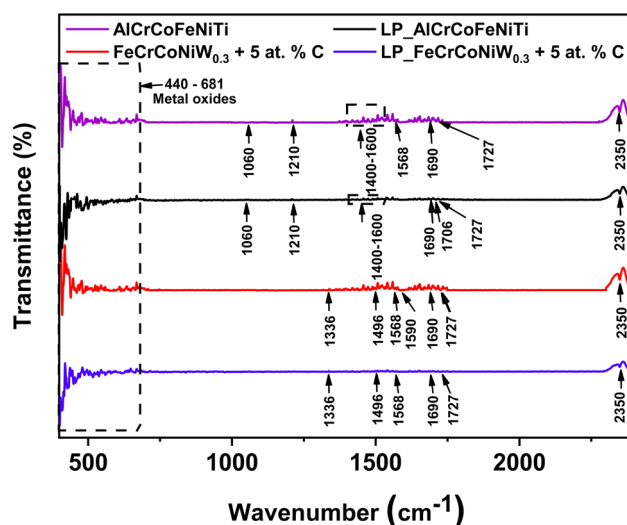


Fig. 13 High resolution FTIR molecular vibrational spectra of AlCrCoFeNiTi and FeCrCoNiW_{0.3} + 5 at.% C APS coatings before and after laser processing

such as Fe–O, Cr–O, Co–O, and Ni–O (Ref 53). Shi et al. have revealed that WC exhibits some distinct bands from 1336 cm⁻¹ to 1590 cm⁻¹ (Ref 58). The characteristic peak at 1496 cm⁻¹ wave number represents the C=O stretching mode. The vibrational spectra at 1568 and 1690 cm⁻¹ corresponded to C=O asymmetric stretching, and C=O stretching mode, respectively. The peaks present at 2350 cm⁻¹ signify the presence of the –O–C–O– group (Ref 57). The LP_FeCrCoNiW_{0.3} + 5% C sample does not deviate from the value assigned to the as-sprayed sample. It shows a peak at 1727 cm⁻¹ associated with C=O asymmetric stretching. The XPS and FTIR results confirm that there are no compositional changes in the LP_FeCrCoNiW_{0.3} + 5% C sample before and after laser processing.

Physical Properties

As illustrated in Fig. 14, the microhardness is evaluated at the coating and substrate cross-section. The microhardness is measured at five different locations in the same region, and the average microhardness is reported. The average microhardness of LP_AlCrCoFeNiTi and LP_FeCoCrNiW_{0.3} + 5 at.% C is calculated as 792 ± 24 HV_{0.2}, and 410 ± 16 HV_{0.2}, respectively. An average microhardness is used since the phase in the alloys has a small size distribution. The LP_AlCrCoFeNiTi had substantially higher microhardness attributed to a sprayed sample due to many reasons. Laser processing reduces porosity and homogeneity in the microstructure, enhancing surface hardness. The increase in hardness is attributed to the development of the BCC phase and the dissolution of the FCC phase upon laser processing, as shown by the XRD findings. The BCC2 phase exhibits a greater weight ratio than the BCC1 phase,

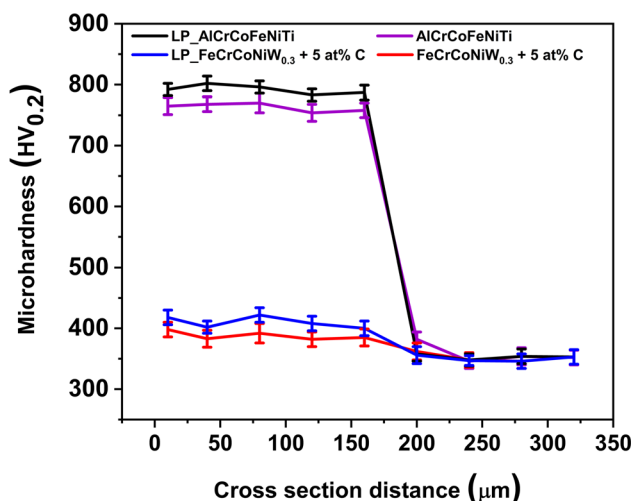


Fig. 14 Microhardness results of the AlCrCoFeNiTi and FeCoCrNiW_{0.3} + 5 at.% C APS coatings before and after laser processing

according to XRD findings. Greater BCC2 phase content in the alloy is associated with higher hardness (Ref 40). Al and Ti have a larger atomic radius than other elements, resulting in lattice distortion and an increase in hardness for these alloys. This is also true for the LP_FeCrCoNiW_{0.3} + 5 at.% C alloy, where the microhardness has increased because more CrC and WC carbides have formed compared with what was found in the original sprayed coating, as shown by the XRD findings. LP_FeCrCoNiW_{0.3} + 5 at.% C alloy exhibit higher hardness due to diffusion of carbon in Cr and W (Ref 11) upon the laser heating and rapid cooling. It is observed that laser surface processing enhances the microhardness of the as-sprayed AlCrCoFeNiTi and as-sprayed FeCrCoNiW_{0.3} + 5 at.% C alloy From 754 ± 12 HV_{0.2} to 792 ± 24 HV_{0.2} (i.e., 5.03%) and 388 ± 16 HV_{0.2} to 410 ± 16 HV_{0.2} (i.e. 5.67%), respectively. Figure 14 shows the microhardness results of both the alloy before and after laser processing at the coating substrate cross-section region.

The nanoindentation technique is used to investigate the physical properties of AlCrCoFeNiTi and FeCoCrNiW_{0.3} + 5 at.% C HEA coating before and after laser processing. The physical properties of each phase are evaluated under a maximum load of 5000μN, 30 indents are made over each phase, and the average value is reported. Table 4 lists the results of physical properties such as contact depth (*h_c*), contact stiffness (*S*), reduced elastic modulus (*E_r*), and hardness (*H*).The reduced elastic modulus (*E_r*) and hardness (*H*) is obtained using Oliver and Pharr method (Ref 59).

$$E_r = \frac{\sqrt{\pi} S}{\sqrt{A_c} 2} \tag{Eq 2}$$

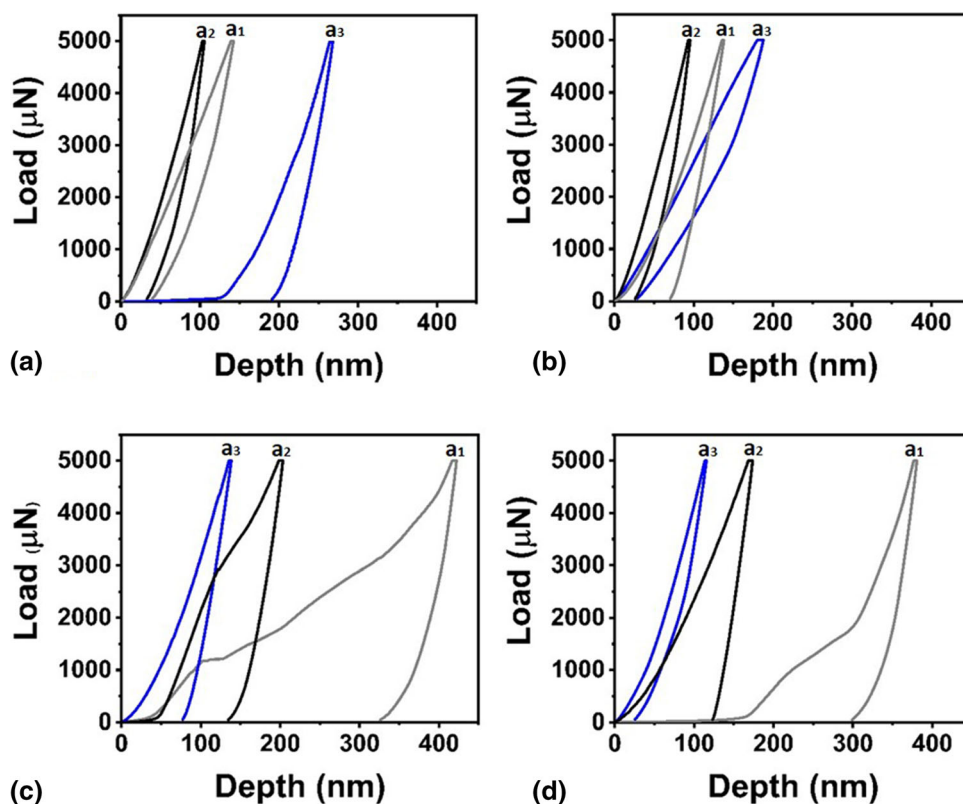
$$H = \frac{P_{max}}{A_c} \tag{Eq 3}$$

where, *S* is the contact stiffness, *A_c* is the projected contact area, and *P_{max}* is the maximum load applied. Load Vs depth curves for both the alloy before and after laser processing are shown in Fig. 15. The a₂B region (Al-rich) exhibits the lower depth, followed by the a₁ region (Ti rich) and a₃ region (Cr-FeNi rich) in the case of AlCrCoFeNiTi and LP_AlCrCoFeNiTi alloy as shown in Fig. 15(a) and (b) respectively. It implies that the a₂ region (rich in Al) is more resistant to plastic deformation in contrast to the a₁ region (rich in Ti) and a₃ region (rich in Cr-Fe-Ni). However, the a₃ region shows lower depth, followed by a₂ and a₁ regions in the case of FeCoCrNiW_{0.3} + 5 at.% C and LP_FeCoCrNiW_{0.3} + 5 at.% C alloy, as shown in Fig. 15(c) and (d), respectively. It infers that the a₃ region (rich in W) has more resistance to plastic deformation in comparison to the a₂ region (rich in Cr) and a₁ region (rich in Fe-Co-Ni). The laser processed both the APS coatings display lower contact depth in contrast to the as-sprayed alloy, which may be attributed due to the formation of various metal oxides at the surface as confirmed by XPS and FTIR results in the preceding section. The average reduced elastic modulus of 90 indents each sample is calculated as 131.42 ± 28 Gpa, 146.66 ± 23 Gpa, 97.51 ± 36 Gpa, and 114.33 ± 24 Gpa for AlCrCoFeNiTi, LP_AlCrCoFeNiTi, FeCoCrNiW_{0.3} + 5 at.% C and LP_FeCoCrNiW_{0.3} + 5 at.% C HEAs, respectively. The average hardness is evaluated as 9.11 ± 5 Gpa, 11 ± 4 Gpa, 6.6 ± 3 and 8.23 ± 3 Gpa for AlCrCoFeNiTi, LP_AlCrCoFeNiTi, FeCoCrNiW_{0.3} + 5 at.% C and LP_FeCoCrNiW_{0.3} + 5 at.% C HEA, respectively.

The LP_AlCrCoFeNiTi and LP_FeCoCrNiW_{0.3} + 5 at.% C HEA display an increase in the average reduced elastic modulus (*E_r*) value with 10.39, 14.71% and average hardness with 17.18 and 19.80%, respectively. The reduced elastic modulus depends upon the crystal structure and the chemistry of the alloy (Ref 60). Adding elements like C changes the ideal shear strength resulting in a change in nanoindentation properties. The lower elastic modulus/hardness or increased elastic modulus/hardness is attributed due to shear instability (Ref 60). The increase in hardness of laser-processed alloy indicates a reduction in plasticity (Ref 32). The difference in hardness between the phases in both alloys is accredited due to composition, phase structure, solidification rate, and oxidation kinetics during the plasma spray and laser processing processes. (Ref 32, 60). The Vickers microhardness value and the nanoindentation hardness have a substantial difference. As compared to microindentation, nanoindentation shows higher hardness values owing to dislocations because of the small indentation area and a comparatively low load of (5000 μN) (Ref 32). Therefore, the nanoindentation findings revealed that laser-treated alloys display higher hardness values that are dependent on phase formation, oxidation state and solidification rate during laser processing (Ref 40).

Table 4 Nanoindentation results of individual phases observed in AlCrCoFeNiTi and FeCoCrNiW_{0.3} + 5 at.% C APS coatings coating before and after laser processing

Alloy	Phase	Maximum load applied (P_{max}), μN	Number of indents (N)	Contact Depth (h_c), nm	Contact Stiffness (S), $\mu\text{N}/\text{nm}$	Reduced Elastic modulus (E_r), Gpa	Hardness (H), Gpa
AlCrCoFeNiTi	a ₁ (Ti rich)	5000	30	134 ± 20	125 ± 10	136 ± 12	10 ± 3
	a ₃ (Cr-Fe-Ni rich)	5000	30	265 ± 63	114 ± 28	98. ± 23	5 ± 2
	a ₂ (Al rich)	5000	30	103 ± 25	86 ± 12	159 ± 49	11 ± 9
LP_AlCrCoFeNiTi	a ₁ (Ti rich)	5000	30	125 ± 42	114 ± 34	147 ± 26	11 ± 6
	a ₃ (Cr-Fe-Ni rich)	5000	30	182 ± 23	94 ± 23	123 ± 35	8 ± 3
	a ₂ (Al rich)	5000	30	97 ± 24	64 ± 8	167 ± 34	14 ± 4
FeCrCoNiW _{0.3} + 5 at.% C	a ₁ (Fe-Ni rich)	5000	30	491 ± 44	129 ± 12	47 ± 30	2 ± 1
	a ₂ (Cr-Fe rich)	5000	30	185 ± 63	95 ± 28	103 ± 49	8 ± 3
	a ₃ (W rich)	5000	30	127 ± 68	70 ± 15	141 ± 29	10 ± 4
LP_FeCrCoNiW _{0.3} + 5 at.% C	a ₁ (Fe-Ni-Cr rich)	5000	30	382 ± 53	124 ± 15	60 ± 23	3 ± 2
	a ₂ (Cr-Fe rich)	5000	30	168 ± 42	111 ± 13	127 ± 18	8 ± 5
	a ₃ (W rich)	5000	30	113 ± 23	72 ± 14	156 ± 27	13 ± 4

Fig. 15 Load-depth curve of (a) AlCrCoFeNiTi, (b) LP_AlCrCoFeNiTi, (c) FeCoCrNiW_{0.3} + 5 at.% C and (d) LP_FeCoCrNiW_{0.3} + 5 at.% C APS coatings

Tribological Properties

In the dry sliding environment with a load of 5 N, the wear behavior of both alloy samples i.e. before and after laser processing is studied at room temperature (25 °C). The wear volume loss is calculated from the wear track profile using

optical microscope as $14 \times 10^{-4} \text{ mm}^3$, $8.9 \times 10^{-4} \text{ mm}^3$, $38.9 \times 10^{-4} \text{ mm}^3$ and $23.45 \times 10^{-4} \text{ mm}^3$ in case of AlCrCoFeNiTi, LP_AlCrCoFeNiTi, FeCrCoNiW_{0.3} + 5 at.% C and LP_FeCrCoNiW_{0.3} + 5 at.% C APS coating, respectively. The volume wear rate of all the samples is calculated and shown in Fig. 16. The volume wear rate calculated is

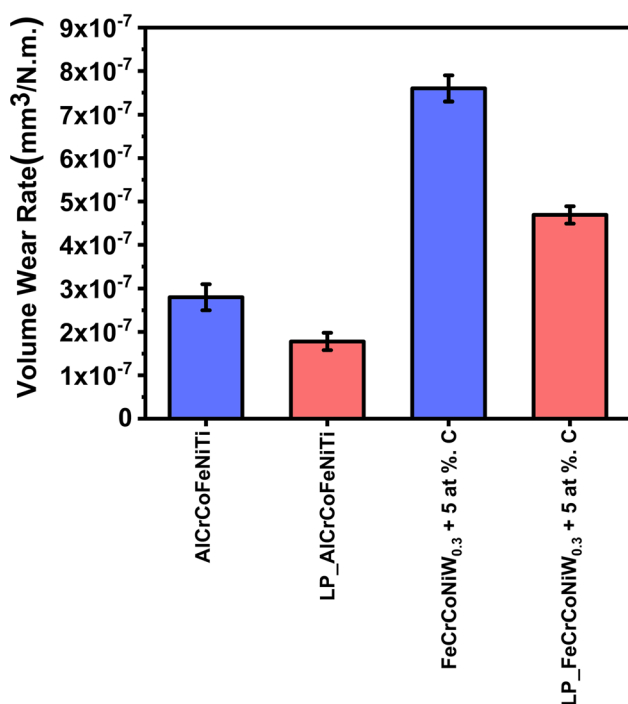


Fig. 16 Volume wear rate of AlCrCoFeNiTi and FeCrCoNiW_{0.3} + 5 at.% C APS coatings before and after laser processing

2.8×10^{-7} , 1.78×10^{-7} , 7.78×10^{-7} and 4.69×10^{-7} mm³/N.m for AlCrCoFeNiTi, LP_AlCrCoFeNiTi, FeCrCoNiW_{0.3} + 5 at.% C and LP_FeCrCoNiW_{0.3} + 5at.% C APS coating, respectively. The LP_AlCrCoFeNiTi alloy has a 36.42% reduced wear volume loss in comparison to the as-sprayed sample. In addition, LP_FeCrCoNiW_{0.3} + 5 at.% C sample revealed a substantial reduction of 39.71% in wear volume loss compared to the APS sample, which can be attributed to the formation of hard carbides during the laser processing as suggested by the XPS and XRD results. Lower volume loss in the wear resistance test makes evident the superior wear resistance property of the LP_AlCrCoFeNiTi APS coating sample. The rapid phase change from solid to liquid to solid is facilitated by laser processing increasing the sample's hardness and wear resistance. Laser processing is also attributed to the lower wear volume loss under dry sliding conditions because of the formation of new BCC phases and CrC and WC phases revealed by XRD. The average increase in the hardness value of 5.03 and 5.67% was attributed to the reduction in volume loss of 36.42 and 39.71% in both the laser-processed samples and follows Archard's law (Ref 34). Laser surface processing increases the hardness of both alloys, and their wear resistance indicates that laser surface processing is an efficient way to improve the wear performance of coatings.

Figure 17 shows the coefficient of friction (COF) curve for as-sprayed and laser-treated AlCrCoFeNiTi and FeCrCoNiW_{0.3} + 5 at.% C APS coatings. The average

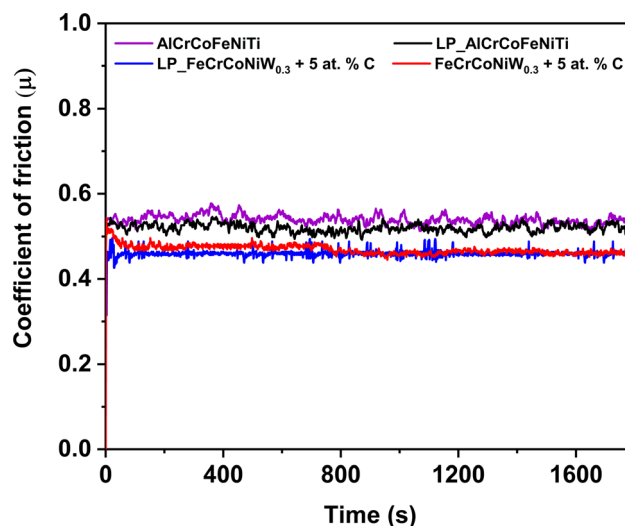


Fig. 17 Coefficient of Friction curve of AlCrCoFeNiTi and FeCrCoNiW_{0.3} + 5 at.% C APS coatings before and after laser processing under a load of 5 N

friction coefficient of the AlCrCoFeNiTi alloy before and after laser processing is 0.46 and 0.45, respectively. Similarly, the average coefficient value for the FeCrCoNiW_{0.3} + 5 at.% C APS coating before and after laser processing was calculated as 0.53 and 0.52, respectively. Laser processed alloys sample exhibit a significant decrease in the coefficient of friction value attributed due to the higher hardness value (Ref 40). The initial rapid increase in the coefficient of friction observed in Fig. 17 can be due to the change in contact area between the tribo pair. After 230–330 s of testing the COF curve reaches equilibrium owing to the increased contact area and decreased contact pressure (Ref 61) between the tribo pair. The development and breakdown of the oxide layer on the surface of the samples leads to the observed fluctuations in the COF (Fig. 17). Over time, the tribo pair heats up, forming an oxide layer that reduces COF and the XPS and FTIR suggests the development of the oxide layer (Fig. 11, 12 and 13). As the test continues, the oxide layer thins and eventually breaks, increasing the COF value. Although oxide production and braking cause COF curve variation, sliding velocity and applied load also play a role. A low coefficient of friction was found in the laser processing of both alloys.

The results of FESEM analysis is presented in Fig. 18. It is used to investigate the wear mechanism in both alloy samples before and after laser treatment. AlCrCoFeNiTi alloy wear morphology showed the presence of an adhesive wear mechanism Fig. 18(a) with exfoliation of the hard particle. Micro scratches are a result of the coating's abrasiveness. On the worn surface, there are a few grooves that may be ascribed to particle pull-out. Less surface damage is seen in LP_AlCrCoFeNiTi APS coated sample,

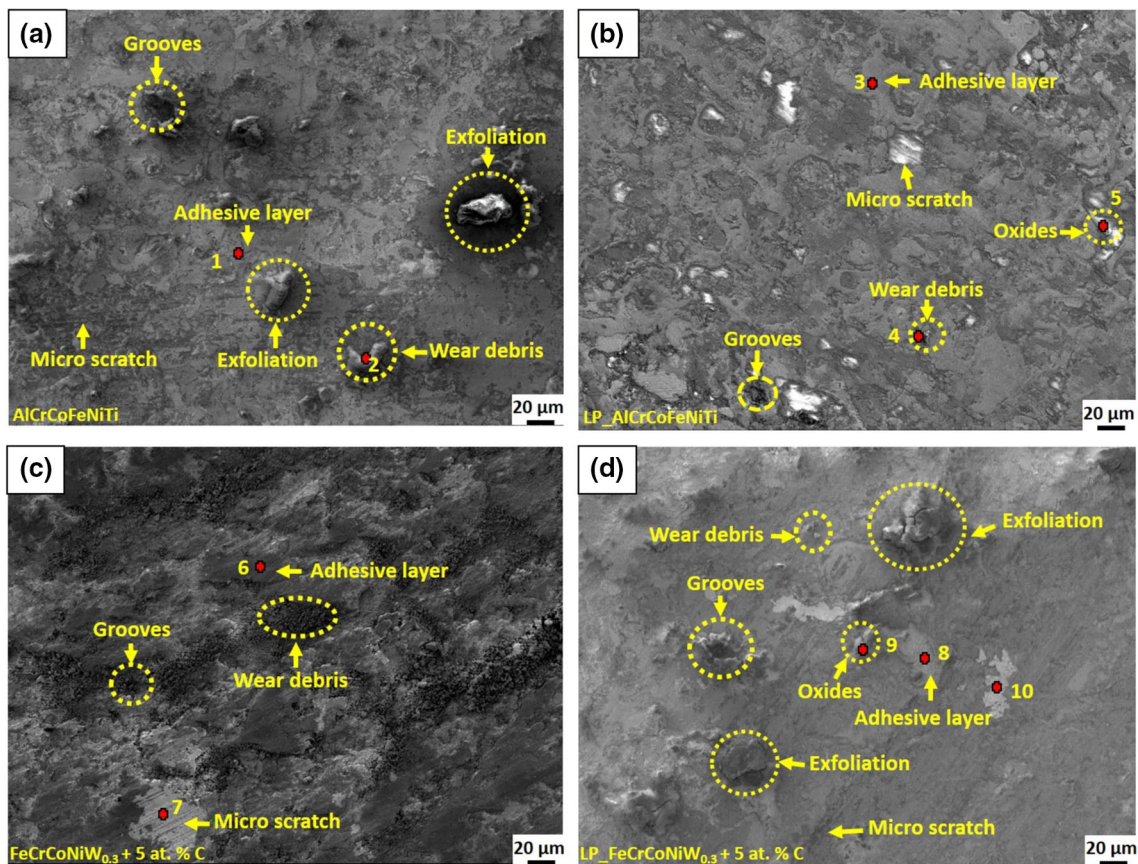


Fig. 18 Worn surface morphology of (a) as sprayed AlCrCoFeNiTi, (b) LP_ AlCrCoFeNiTi, (c) as sprayed FeCrCoNiW_{0.3} + 5 at.% C alloy and (d) LP_ FeCrCoNiW_{0.3} + 5 at.% C APS coatings

as shown in Fig. 18(b), compared to the as-sprayed sample, as shown in Fig. 18(a). The decreased friction coefficient may be caused by the rolling of abrasive wear debris (Ref 40). An increase in temperature causes the oxide layer to develop and break, changing the friction coefficient abruptly. The wear debris moving between the ball and the sample reduces the coefficient of friction in LP_ AlCrCoFeNiTi APS coating. Besides, wear debris accelerates the three-body abrasive wear. The micro scratch confirms the abrasive wear mechanism. Abrasion and adhesion are the primary wear mechanisms observed in LP_ AlCrCoFeNiTi HEA. However, FeCrCoNiW_{0.3} + 5 at.% C APS coated samples exhibit adhesive wear with more surface damage attributed to the lower hardness value and confirm the higher coefficient of friction, as shown in Fig. 18(c). The presence of grooves was attributed to the removal of the WC particle that was embedded in it. Abrasive wear is demonstrated by the micro scratches. In LP_ FeCrCoNiW_{0.3} + 5 at.% C APS coated samples, adhesive, abrasive, and oxide wear mechanisms predominate, as shown in Fig. 18(d). Only a few grooves formed in

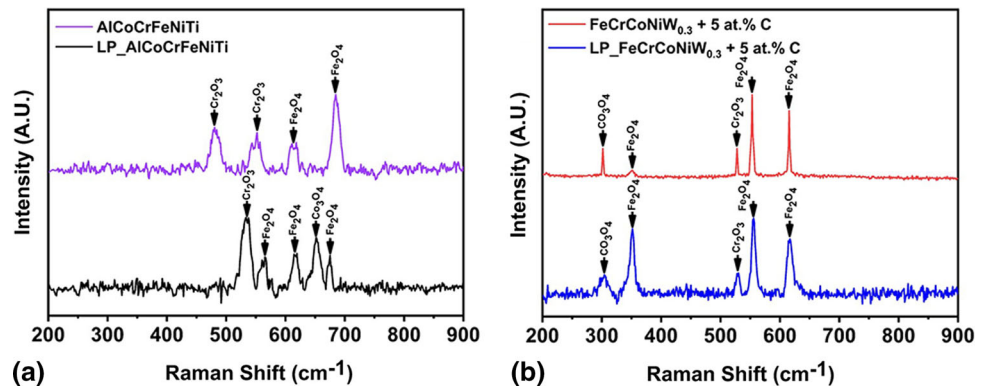
the LP_ FeCrCoNiW_{0.3} + 5 at.% C alloy after laser surface processing, which may have been produced by a hard particle (Carbides) pulled out during the wear test. The exfoliation of hard particles was also observed in the wear track, which can be attributed to abrasive wear. As a result of its lower surface roughness, higher hardness, superior wear resistance, and lower coefficient of friction, laser processing can be used to improve the surface and mechanical properties of coatings in aerospace and naval applications.

EDS analysis was conducted on worn surfaces at different locations highlighted in Fig. 18(a), (b), (c) and (d). The findings of the EDS analysis demonstrate the presence of metal oxides on the worn surfaces. The oxygen content in the adhesive layer of the as-sprayed alloy is 29.54%, with a high concentration of Al, Cr, and Ti and a low concentration of Co and Ni. Laser-processed alloys reveal the presence of metal oxide spots, as illustrated in Fig. 18(b) and (c), which indicate the development of oxide layers (d). The oxides spots of LP_ AlCrCoFeNiTi and LP_ FeCrCoNiW_{0.3} + 5 at.% C APS coatings, as

Table 5 EDS analysis result of the worn surface at various locations highlighted in Fig. 18

EDS Locations	Elements (at.%)							
	Al	Co	Cr	Fe	Ni	Ti	W	O
1 in Fig. 18 a	15.32	4.63	14.62	14.24	7.03	14.62	...	29.54
2 in Fig. 18 a	13.25	6.52	11.29	10.52	7.63	16.27	...	34.52
3 in Fig. 18 b	12.35	5.82	12.52	15.03	5.93	13.83	...	34.52
4 in Fig. 18 b	39.63	8.11	6.45	5.73	6.36	5.16	...	28.56
5 in Fig. 18 b	10.34	4.69	10.41	10.95	4.76	12.64	...	46.21
6 in Fig. 18 c	...	8.68	24.79	21.92	6.44	...	7.83	30.34
7 in Fig. 18 c	...	4.33	4.35	3.96	3.93	...	64.89	18.54
8 in Fig. 18d	...	9.72	22.54	14.49	9.85	...	4.84	38.56
9 in Fig. 18 d	...	6.32	18.34	12.43	8.77	...	6.62	47.52
10 in Fig. 18 d	...	1.25	2.6	2.43	1.11	...	68.54	24.07

Fig. 19 Raman spectra of AlCrCoFeNiTi and FeCrCoNiW_{0.3} + 5 at.% C APS coatings before and after laser treatments on the worn surfaces



shown in Fig. 18(b) and (d), respectively, have a higher oxygen concentration of 46.21 and 47.52%. The EDS analysis of the wear debris (Table 5) suggests the presence of all the metals as well as oxygen.

Additionally, Raman spectroscopy was used to examine the worn surfaces of both APS coatings before and after laser processing to identify the oxidation states and the type of oxides developed. Figure 19 shows the Raman spectra of both APS coatings before and after laser processing. The Raman spectra of AlCrCoFeNiTi coating as shown in Fig. 19(a) display the four distinct peaks at 480.9, 553.04, 614.80 and 684.8 cm⁻¹ can be allocated to the Cr₂O₃, Cr₂O₃, Fe₂O₄ and Fe₂O₄, respectively (Ref 27, Ref 62–64). The characteristics spectra of LP_AlCrCoFeNiTi APS coating display five different peaks at 535.2, 565.4, 615.73, 651.43 and 674.43 can be associated with Cr₂O₃, Fe₂O₄, Fe₂O₄, Co₃O₄, and Fe₂O₃ correspondingly (Ref 62–65, Ref 27). The characteristics spectrum of LP_AlCrCoFeNiTi APS coating exhibit similar peaks as AlCrCoFeNiTi APS coating. However, AlCrCoFeNiTi alloy show the higher relative intensity of Fe₂O₄, and LP_AlCrCoFeNiTi APS coating shows the higher relative intensity of Cr₂O₃ in comparison to each other. Raman spectra of FeCrCoNiW_{0.3} + 5 at.% C APS coating exhibit the six distinct peaks at 303.8, 351.9, 528.8, 555.8, and 614.8 cm⁻¹

can be assigned to Co₃O₄, Fe₂O₄, Cr₂O₃, Fe₂O₃, and Fe₂O₄, respectively (Ref 62–64) as shown in Fig. 19(b). The characteristics spectrum of LP_FeCrCoNiW_{0.3} + 5 at.% C APS coating exhibit similar peaks as FeCrCoNiW_{0.3} + 5 at.% C APS coating with higher relative intensity of Fe₂O₄ in compare to Cr₂O₃ and Co₃O₄. Therefore, Raman spectroscopy revealed the presence of Cr₂O₃, Fe₂O₄, TiO₂, and Co₃O₄ kinds of oxides, which is consistent with EDS findings. Higher oxygen concentration in the laser-processed alloy improves the wear resistance and reduces the tribo pair adhesion due to self-lubricating properties (Ref 32).

Summary and Conclusions

AlCrCoFeNiTi and FeCrCoNiW_{0.3} + 5 at.% C APS coatings were treated utilizing the laser surface processing technique. The effect of laser surface processing on both materials was thoroughly investigated. The research came to the following outcome.

- Laser processing attributed to decrease in the surface roughness (Sa) of LP_AlCrCoFeNiTi and LP_FeCrCoNiW_{0.3} + 5 at.% C alloy coatings by 29.03% and 29.59%, respectively.

- After laser processing, more BCC phases evolved with the depletion of minor FCC phase in LP_AlCrCoFeNiTi HEA and more CrC and WC hard phases evolved in LP_FeCrCoNiW_{0.3} + 5 at.% C HEA coating.
- The dilution percentage were calculated as 9.43% and 8.41% for LP_AlCrCoFeNiTi and LP_FeCrCoNiW_{0.3} + 5 at.% C HEAs. They exhibit good metallurgical bonding between coating and substrate.
- The average microhardness was improved after laser processing by 5.03% and 5.67% in LP_AlCrCoFeNiTi and LP_FeCrCoNiW_{0.3} + 5 at.% C HEAs, respectively.
- Nanoindentation results suggest that both the HEAs i.e. AlCrCoFeNiTi and FeCoCrNiW_{0.3} + 5 at.% C, have an increase in the average reduced elastic modulus (E_r) of 10.39 and 14.71%, respectively. In addition, the average hardness also increased by 17.18 and 19.80%, respectively post laser processing. The Al-rich phase of AlCrCoFeNiTi exhibit a higher hardness value, and the W-rich phase of FeCoCrNiW_{0.3} + 5 at.% C exhibits a higher hardness
- The wear volume is significantly reduced by 37.32 and 39.71% in LP_AlCrCoFeNiTi and LP_FeCrCoNiW_{0.3} + 5 at.% C alloy post laser processing, the wear mechanism involved is a combination of adhesive and abrasive in nature with oxide formation. The results suggest that the alloy can be potentially used for wear resistance applications.

However, the high temperature phase stability of laser treated alloy is still not well understood. Studies in this area would help in further adapting the aforementioned alloys for the multitude of high temperature applications i.e. aerospace, metallurgy, automobile, etc.

Acknowledgements This research work is financially supported by the Indian Space Research Organization (ISRO) under project no. (ISRO/RES/3/844/19-20). The authors like to express their gratitude to ISRO for funding this project. The authors extend their gratitude to the central instrumentation facility (CIF) at Indian Institute of Technology Jammu (IIT Jammu) for providing the essential characterization facility.

Funding This study was funded by Indian Space Research Organization (ISRO) (Grant no. ISRO/RES/3/844/19-20).

Conflict of interests Author S. Shiva has received research grants from Indian Space Research Organization (ISRO). The authors declare that they have no conflict of interest.

References

1. J.W. Yeh, S.K. Chen, S.J. Lin, J.Y. Gan, T.S. Chin, T.T. Shun, C.H. Tsau and S.Y. Chang, Nanostructured High-Entropy Alloys with Multiple Principal Elements: Novel Alloy Design Concepts and Outcomes, *Adv. Eng. Mater.*, 2004, **6**, p 299-303.
2. B. Cantor, I.T.H. Chang, P. Knight and A.J.B. Vincent, Microstructural Development in Equiatomic Multicomponent Alloys, *Mater. Sci. Eng. A*, 2004, **375**, p 213-218.
3. H. Liu, J. Liu, Xi. Li, P. Chen, H. Yang and J. Hao, Effect of Heat Treatment on Phase Stability and Wear Behavior of Laser Clad AlCoCrFeNiTi_{0.8} High-Entropy Alloy Coatings, *Surf. Coat. Technol.*, 2020, **392**, p 125758. <https://doi.org/10.1016/j.surfcoat.2020.125758>
4. M. Löbel, T. Lindner and T. Lampke, High-Temperature Wear Behaviour of AlCoCrFeNiTi_{0.5} Coatings Produced by HVOF, *Surf. Coat. Technol.*, 2020, **403**, p 126379. <https://doi.org/10.1016/j.surfcoat.2020.126379>
5. Xu. Zhen, D.Y. Li and D.L. Chen, Effect of Ti on the Wear Behavior of AlCoCrFeNi High-Entropy Alloy During Unidirectional and Bi-Directional Sliding Wear Processes, *Wear*, 2021, **476**, p 203650. <https://doi.org/10.1016/j.wear.2021.203650>
6. P.S. Sujit Das and Robi, A Novel Refractory WmVCrTa High-Entropy Alloy Possessing Fine Combination of Compressive Stress-Strain and High Hardness Properties, *Adv. Powder Technol.*, 2020, **31**(12), p 4619-4631. <https://doi.org/10.1016/j.apt.2020.10.008>
7. P. Niu, R. Li, S. Zhu, M. Wang, C. Chen and T. Yuan, Hot Cracking, Crystal Orientation and Compressive Strength of an Equimolar CoCrFeMnNi High-Entropy Alloy Printed by Selective Laser Melting, *Opt Laser Technol.*, 2020, **127**, p 10614.
8. H. Jiang, D. Qiao, Lu. Yiping, Z. Ren, Z. Cao, T. Wang and T. Li, Direct Solidification of Bulk Ultrafine-Microstructure Eutectic High-Entropy Alloys with Outstanding Thermal Stability, *Scr. Mater.*, 2019, **165**, p 145-149.
9. Fu. Wujing, W. Zheng, Y. Huang, F. Guo, S. Jiang, P. Xue, Y. Ren, H. Fan, Z. Ning and J. Sun, Cryogenic Mechanical Behaviors of CrMnFeCoNi High-Entropy Alloy, *Mater. Sci. Eng. A.*, 2020, **789**, 139579.
10. H. Wang, Q. Liu, Y. Guo and H. Lan, MoFe_{1.5}CrTiWAlNb_x Refractory High-Entropy Alloy Coating Fabricated by Laser Cladding, *Intermetallics*, 2019, **115**, p 106613. <https://doi.org/10.1016/j.intermet.2019.106613>
11. M.G. Poletti, G. Fiore, F. Gili, D. Mangherini and L. Battezzati, Development of a New High Entropy Alloy for Wear Resistance: FeCoCrNiW_{0.3} and FeCoCrNiW_{0.3}+5at. % of C, *Mater. Des.*, 2017, **115**, p 247-254.
12. R. Zhou, G. Chen, B. Liu, J. Wang, L. Han and Y. Liu, Microstructures and Wear Behaviour of (FeCoCrNi)_{1-x}(WC)_x High Entropy Alloy Composites, *Int. J. Refract Met H.*, 2018, **75**, p 56-62.
13. Z. Wu, H. Bei, G.M. Pharr and E.P. George, Temperature Dependence of the Mechanical Properties of Equiatomic Solid Solution Alloys with Face-Centered Cubic Crystal Structures, *Acta Mater.*, 2014, **81**, p 428-441.
14. T. Nguyen, X. Ly, M. Huang, Y. Qin and S. Yang, Fabrication and Characterization of Al_xFeMnNiCrCu_{0.5}(x = 0.0; 0.5; 1.0) High-Entropy Alloy Coatings by Laser Cladding, *J. Therm. Spray Technol.*, 2022, **31**(4), p 980-990. <https://doi.org/10.1007/s11666-022-01346-8>
15. A. Verma, P. Tarate, A.C. Abhyankar, M.R. Mohape, D.S. Gowtam, V.P. Deshmukh and T. Shanmugasundaram, High Temperature Wear in CoCrFeNiCux High Entropy Alloys: the Role of Cu, *Scripta Mater.*, 2019, **161**, p 28-31.
16. G.A. Salishchev, M.A. Tikhonovsky, D.G. Shaysultanov, N.D. Stepanov, A.V. Kuznetsov, I.V. Kolodiy, A.S. Tortika and O.N. Senkov, Effect of Mn and V on Structure and Mechanical Properties of High-Entropy Alloys based on CoCrFeNi System, *J. Alloys Compd.*, 2014, **591**, p 11-21.
17. G. Liang, G. Jin, X. Cui, Z. Qiu and J. Wang, The Directional Array TiN-Reinforced AlCoCrFeNiTi High-Entropy Alloy Synthesized in situ via Magnetic Field-Assisted Laser Cladding, *Appl. Surf. Sci.*, 2022, **572**, 151407.

18. B. Gwalani and V. Soni, Owais Ahmed Waseem, Srinivas Aditya Mantri, Rajarshi Banerjee, Laser Additive Manufacturing of Compositionally Graded AlCrFeMoVx (x = 0 to 1) High-Entropy Alloy System, *Opt. Laser Technol.*, 2019, **113**, p 330-337.
19. L. Ding and H. Wang, Microstructure and Wear Resistance of Laser Clad CoCrFeNiTiNbBx High Entropy Alloy Coatings, *J. Therm. Spray Tech.*, 2021, **30**, p 2187-2196.
20. W. Wu, L. Jiang, H. Jiang et al., Phase Evolution and Properties of Al2CrFeNiMo x High-Entropy Alloys Coatings by Laser Cladding, *J Therm Spray Tech.*, 2015, **24**, p 1333-1340.
21. Y. Yu, J. Wang, J.S. Li, H.C. Kou and W.M. Liu, Characterization of BCC Phases in AlCoCrFeNiTiX High Entropy Alloys, *Mater.Lett.*, 2015, **138**, p 78-80.
22. J.M. Park, J. Moon, J.W. Bae, J. Jung, S. Lee and H.S. Kim, Effect of Annealing Heat Treatment on Microstructural Evolution and Tensile Behaviour of Al0.5CoCrFeMnNi High-Entropy Alloy, *Mater. Sci. Eng. A*, 2018, **728**, p 251–258.
23. Z. Fu, W. Chen, Z. Chen, H. Wen and E.J. Lavernia, Influence of Ti Addition and Sintering Method on Microstructure and Mechanical Behaviour OF A Medium-Entropy Al0.6CoNiFe Alloy, *Mater. Sci. Eng. A*, 2014, **619**, p 137-145.
24. D. Kong, J. Guo, R. Liu, X. Zhang, Y. Song, Z. Li, F. Guo, X. Xing, Xu. Yuan and W. Wang, Effect of Remelting and Annealing on the Wear Resistance of AlCoCrFeNiTi05 High Entropy Alloys, *Intermetallics*, 2019, **114**, p 106560.
25. Benbin Xin, Aijun Zhang, Jiasheng Han, Bo Su, Junhu Meng (2020) Tuning composition and microstructure by doping Ti and C for enhancing mechanical property and wear resistance of Al0.2Co15CrFeNi1.5Ti05 high entropy alloy matrix composites, *J. Alloys Compd.*, , **836**, p 155273
26. A. Meghwal, A. Anupam, B.S. Murty et al., Thermal Spray High-Entropy Alloy Coatings: A Review, *J Therm Spray Tech.*, 2020, **2020**(29), p 857-893.
27. P. Patel, S.A. Alidokht, N. Sharifi et al., Microstructural and Tribological Behavior of Thermal Spray CrMnFeCoNi High Entropy Alloy Coatings, *J Therm Spray Tech.*, 2022, **31**, p 1285-1301.
28. X. Liu, F. Lv, H. Li et al., Microstructure and High-Temperature Tribological Behavior of Plasma-Sprayed FeCoCrAlNi High Entropy Alloy Coatings Under Higher Load Condition, *J Therm Spray Tech*, 2022, **31**, p 1276-1284.
29. J. Mahaffey, A. Vackel, S. Whetten et al., Structure Evolution and Corrosion Performance of CoCrFeMnNi High Entropy Alloy Coatings Produced Via Plasma Spray and Cold Spray, *J. Therm. Spray Tech.*, 2022, **31**, p 1143-1154.
30. X. Ma, P. Ruggiero, R. Bhattacharya et al., Evaluation of New High Entropy Alloy as Thermal Sprayed Bondcoat in Thermal Barrier Coatings, *J. Therm. Spray Tech.*, 2022, **31**, p 1011-1020.
31. F. Ghadami, S. Ghadami and M.A. Davoudabadi, Sliding Wear Behavior of the Nanoceria-Doped AlCrFeCoNi High-Entropy Alloy Coatings Deposited by Air Plasma Spraying Technique, *J Therm Spray Tech*, 2022, **31**, p 1263-1275.
32. A. Meghwal, A. Anupam, V. Luzin, C. Schulz, B.S. Colin Hall, R.S. Murty, C.C. Kottada, A.S. Berndt and M. Ang, Multiscale Mechanical Performance and Corrosion Behaviour of Plasma Sprayed AlCoCrFeNi High-Entropy Alloy Coatings, *J. Alloys Compound.*, 2021, **854**, p 157140. <https://doi.org/10.1016/j.jallcom.2020.157140>
33. H. Kumar, G.A. Bhaduri, S.G.K. Manikandan, M. Kamaraj and S. Shiva, Influence of Annealing on Microstructure and Tribological Properties of AlCoCrFeNiTi High Entropy Alloy Based Coating, *Metals Mater. Inter.*, 2022 <https://doi.org/10.1007/s12540-022-01264-y>
34. H. Kumar, G.A. Bhaduri, S.G.K. Manikandan et al., Microstructural Characterization and Tribological Properties of Atmospheric Plasma Sprayed High Entropy Alloy Coatings, *J Therm Spray Tech.*, 2022, **31**, p 1956-1974.
35. R.S. Kiplangat, T.-T. Lin, N.G. Kipkirui and S.-H. Chen, Microstructure and Mechanical Properties of the Plasma-Sprayed and Cold-Sprayed Al0.5CoCrFeNi2Ti0.5 High-Entropy Alloy Coatings, *J Therm Spray Technol*, 2022, **31**(4), p 1207-1221. <https://doi.org/10.1007/s11666-022-01356-6>
36. L. Tian, J. Wang, Q. Zhang, R. Li and C. Liu, Microstructure Characterization of AlCoCrFeNiTi High-Entropy Alloy Coating Produced by Atmospheric Plasma Spraying, *Mater. Res. Express*, 2019, **6**, 116416.
37. H. Kumar, S.G.K. Chandra Kumar, M. Manikandan and S.S. Kamaraj, Laser Re-Melting of Atmospheric Plasma Sprayed High Entropy Alloy, *Advanced Engineering of Materials Through Lasers*. J. Radhakrishnan, S. Pathak Ed., Springer International Publishing, Cham, 2022, p 105-127. https://doi.org/10.1007/978-3-031-03830-3_5
38. K.M. Doleker, The Examination of Microstructure and Thermal Oxidation Behavior of Laser-Remelted High-Velocity Oxygen Liquid Fuel Fe/Al Coating, *J. Materi Eng Perform.*, 2020, **29**, p 3220–3232.
39. X. Wei, P. Zhang, Yu. Zhishui, H. Yan, Wu. Di, H. Shi, J. Chen, Lu. Qinghua, Y. Tian, S. Ma and W. Lei, Effect of Phase Transformation on Mechanical Properties of Al16.80Co20.74Cr20.49Fe21.28Ni20.70 High Entropy Alloy Coatings Processed by Laser Cladding, *J. Alloys Comp.*, 2021, **862**, p 158563. <https://doi.org/10.1016/j.jallcom.2020.158563>
40. A. Erdogan, Kadir Mert Döleker, Sakin Zeytin, Effect of Laser Remelting on Electric Current Assistive Sintered CoCrFeNiAlxTiY High Entropy Alloys: Formation, Micro-Hardness and wear Behaviors, *Surf. Coat. Technol.*, 2020, **399**, 126179.
41. K.M. Doleker, A. Erdogan and S. Zeytin, Laser Re-Melting Influence on Isothermal Oxidation Behavior of Electric Current Assisted Sintered CoCrFeNi, CoCrFeNiAl0.5 and CoCrFeNiTi0.5Al0.5 High Entropy Alloys, *Surf. Coat. Technol.*, 2021, **407**, p 126775. <https://doi.org/10.1016/j.surfcoat.2020.126775>
42. C. Wang, Yu. Jianxing, Yu. Zhang and Yu. Yang, Phase Evolution and Solidification Cracking Sensibility in Laser Remelting Treatment of the Plasma-Sprayed CrMnFeCoNi High Entropy Alloy Coating, *Mater. Des.*, 2019, **182**, 108040.
43. L. Salvati, L.E. Makovsky, J.M. Stencil, F.R. Browns and D.M. Hercules, Surface Spectroscopic Study of Tungsten-Alumina Catalysts Using X-ray Photoelectron, Ion Scattering, and Raman Spectroscopies, *J. Phys. Chem.*, 1981, **85**, p 3700-3707.
44. J.R. Lindsay, H.J. Rose, W.E. Swartz, P.H. Watts and K.A. Rayburn, X-Ray Photoelectron Spectra of Aluminum Oxides: Structural Effects on the "Chemical Shift", *Appl. Spectrosc.*, 1973, **27**, p 1-5.
45. C.-M. Chan, S. Trigwell and T. Duerig, Oxidation of an NiTi Alloy, *Surf. Inter. Anal.*, 1990, **15**(6), p 349-354. <https://doi.org/10.1002/sia.740150602>
46. M.C. Biesinger, B.P. Payne, A.P. Grosvenor, L.W.M. Lau, A.R. Gerson and R.S.C. Smart, Resolving Surface Chemical States in XPS Analysis of First Row Transition Metals, Oxides and Hydroxides: Cr, Mn, Fe, Co and Ni, *Appl. Surf. Sci*, 2011, **257**, p 2717–2730.
47. C. Sarra-Bournet, B. Haberl, C. Charles and R. Boswell, Characterization of Nanocrystalline Nitrogen-Containing Titanium Oxide Obtained by N2/O2/Ar Low-Field Helicon Plasma Sputtering, *J. Phys. D: Appl. Phys.*, 2011, **44**, 455202.
48. S. Mischler, H.J. Mathieu and D. Landolt, The Investigation of Passive Films on Iron—Chromium Alloys by AES and XPS, *Surf. Interface Anal.*, 1988, **12**, p 429-429.
49. G.A. Bhaduri and L. Šiller, Nickel Nanoparticles Atalyse Reversible Hydration of Carbon Dioxide for Mineralization Carbon Capture and Storage, *Catal. Sci. Technol.*, 2013, **3**, p 1234-1239.
50. S.M. Schmuecker, D. Clouser, T.J. Kraus and B.M. Leonard, Synthesis of Metastable Chromium Carbide Nanomaterials and

- their Electrocatalytic Activity for the Hydrogen Evolution Reaction, *Dalt. Trans.*, 2017, **46**, p 13524–21353.
51. P.S. Bagus, C.J. Nelin, C.R. Brundle, B.V. Crist, N. Lahiri and K.M. Rosso, Combined Multiplet Theory and Experiment for the Fe 2p and 3p XPS of FeO and Fe₂O₃, *J. Chem. Phys.*, 2021, **154**, 094709.
 52. B. Li, D. Li, T. Mei, W. Xia and W. Zhang, Fabrication and Characterization of Boron Nitride Reinforced Ni–W Nanocomposite Coating by Electrodeposition, *J. Alloys Compd.*, 2019, **777**, p 1234–1244.
 53. M. Kazemnejadi, Z. Sharafi, B. Mahmoudi et al., Magnetic Fe–Cr–Ni Oxide Alloy Nano-Belts Prepared from the Chemical Decomposition of a Stainless Steel Screw (a top-down approach): an Efficient and Cheap Catalyst for Multicomponent Reactions, *J. Iran. Chem. Soc.*, 2020, **17**, p 777–787.
 54. A. Marin, C.P. Lungu and C. Porosnicu, Influence of Gaseous Environments on Beryllium–Tungsten and Tungsten Surfaces Investigated by XPS, *J. Vac. Sci. Technol. A*, 2017, **35**, p 021403.
 55. C. Liu, K. Shih, Y. Gao et al., Dechlorinating Transformation of Propachlor Through Nucleophilic Substitution by Dithionite on the Surface of Alumina, *J. Soils Sediments*, 2012, **12**, p 724–733.
 56. P. Benjwal, M. Kumar, P. Chamoli and K.K. Kar, Enhanced Photocatalytic Degradation of Methylene Blue and Adsorption of Arsenic (iii) by Reduced Graphene Oxide (rGO)–Metal Oxide (TiO₂/Fe₃O₄) Based Nanocomposites, *RSC Adv.*, 2015, **5**(89), p 73249–73260. <https://doi.org/10.1039/C5RA13689J>
 57. S. Awasthi and R. Singhal, A Mathematical Study on Effect of 2-Hydroxyl Ethyl Acrylate on Controlled Drug Diffusion from Smart Hydrogels Based on Poly(acrylamide-co-hydroxy ethyl acrylate-co-acrylic acid), *J. Macromole. Sci., Part A*, 2012, **49**(5), p 397–413. <https://doi.org/10.1080/10601325.2012.671760>
 58. P. Hoffmann, H. Galindo, G. Zambrano, C. Rincón and P. Prieto, FTIR Studies of Tungsten Carbide in Bulk Material and Thin Film Samples, *Mater. Charact.*, 2003, **50**, p 255–259.
 59. W. Oliver and G. Pharr, Measurement of Hardness and Elastic Modulus by Instrumented Indentation: advances in Understanding and Refinements to Methodology, *J. Mater. Res.*, 2004, **19**(1), p 3–20.
 60. S. Sinha, R.A. Mirshams, T. Wang et al., Nanoindentation Behavior of High Entropy Alloys with Transformation-Induced Plasticity, *Sci Rep.*, 2019, **9**, p 6639.
 61. H. Liu, X. Li, J. Liu, W. Gao, Du. Xiaotong and J. Hao, Microstructural Evolution and Properties of Dual-Layer CoCr–FeMnTi_{0.2} High-Entropy Alloy Coating Fabricated by Laser Cladding, *Opt. Laser Technol.*, 2021, **134**, p 106646.
 62. H. Li, J. Li, C. Yan, X. Zhang and D. Xiong, Microstructure and Tribological Properties of Plasma-Sprayed Al_{0.2}Co_{1.5}CrFe–Ni_{1.5}Ti–Ag Composite Coating from 25 to 750 °C, *J. Mater. Eng. Perform.*, 2020, **29**(3), p 1640–1649. <https://doi.org/10.1007/s11665-020-04700-5>
 63. M.A.G. Soler and F. Qu, *Raman Spectroscopy of Iron Oxide Nanoparticles BT - Raman Spectroscopy for Nanomaterials Characterization*, Springer, Berlin Heidelberg, 2012, p 379–416
 64. A. Motallebzadeh, S.A.A. Dilawary, E. Atar et al., High-Temperature Oxidation of Stellite 12 Hardfacings: Effect of Mo on Characteristics of Oxide Scale, *J. of Materi Eng and Perform.*, 2019, **28**, p 463–474.
 65. J.C. Rubim, M.H. Sousa, J.C.O. Silva and F.A. Tourinho, Raman Spectroscopy as a Powerful Technique in the Characterization of Ferrofluids, *Braz. J. Phys.*, 2001, **31**(3), p 402–408. <https://doi.org/10.1590/S0103-97332001000300010>

Publisher's Note Springer Nature remains neutral with regard to jurisdictional claims in published maps and institutional affiliations.

Springer Nature or its licensor (e.g. a society or other partner) holds exclusive rights to this article under a publishing agreement with the author(s) or other rightsholder(s); author self-archiving of the accepted manuscript version of this article is solely governed by the terms of such publishing agreement and applicable law.